Journal of Chemical Theory and Computation 13 (2017): 992-1009

DOI: http://dx.doi.org/10.1021/acs.jctc.6b00984

M_3C: A Computational Approach to Describe Statistical Fragmentation of Excited Molecules and Clusters

Néstor F. Aguirre[1],[*,†] Sergio Díaz-Tendero[1,4],[†,‡] Paul-Antoine Hervieux[2],[¶] Manuel Alcamí[1,3],[†,§] and Fernando Martín[1,3,4†,§,‡]

†*Departamento de Química, Módulo 13,Universidad Autónoma de Madrid, 28049, Madrid, Spain*

‡*Condensed Matter Physics Center (IFIMAC), Universidad Autónoma de Madrid, 28049 Madrid, Spain.*

¶*Université de Strasbourg, CNRS, Institut de Physique et Chimie des Matériaux de Strasbourg, 67000 Strasbourg, France*

§*Instituto Madrileño de Estudios Avanzados en Nanociencias (IMDEA-Nanociencia), 28049 Madrid, Spain*

E-mail: nestor.aguirre@uam.es

Abstract

The Microcanonical Metropolis Monte Carlo method, based on a random sampling of the density-of-states, is revisited for the study of molecular fragmentation in the gas phase (isolated molecules, atomic and molecular clusters, complex biomolecules, etc). A random walk or uniform random sampling in the configurational space (atomic positions) and a uniform random sampling of the relative orientation, vibrational energy and chemical composition of the fragments is used to estimate the density of states of

the system, which is continuously updated as the random sampling populates individual states. The validity and usefulness of the method is demonstrated by applying it to evaluate the caloric curve of a weakly bound rare gas cluster (Ar_{13}), to interpret the fragmentation of highly excited small neutral and singly-positively-charged carbon clusters (C_n, $n = 5, 7, 9$; and C_n^+, $n = 4, 5$) and to simulate the mass spectrum of the acetylene molecule (C_2H_2).

1 Introduction

High-energy ionic and electronic beams, as well as laser pulses and synchrotron radiation sources, are widely used to investigate the properties and dynamics of complex molecular systems. Bombardment by these particles involves excitation and/or ionization of the molecular target, which ultimately dissociates as a consequence of the excess of energy deposited by the projectile.[1–5] Thus the analysis of the type of fragments resulting from the collision together with their kinematical properties can provide useful information on the parent molecular system, such as its stability against ionization and excitation, its electronic structure and geometrical configuration, the type of interaction between the subunits conforming the cluster/molecule, etc.[6–12] For this, a key point is to understand how the energy deposited on the molecular target is distributed among the various electronic and nuclear degrees of freedom available in the system (electronic, vibrational, rotational and translational) and how this distribution leads in the end to the observed fragmentation.

In this respect, time-resolved experimental studies, as those making use of ultrashort light pulses, can provide a wealth of information about the dynamics of such excited and ionized molecules.[13,14] For example, by using pump-probe schemes, one can infer the motion of holes created after ionization of a biomolecule[15] or follow the nuclear dynamics of charged and excited molecules[16] by measuring fragmentation yields as a function of the pump-probe delay time. In addition to this, new experimental techniques for cluster production and ion storage rings facilitate the study of increasingly more complex systems, such as, e.g., clusters of

fullerenes[17] or clusters of polycyclic aromatic hydrocarbons.[18] However, the full reconstruction of the properties and evolution of complex molecular targets from such time resolved measurements is still very challenging due to the large number of accessible fragmentation channels, which requires the use of sophisticated multicoincidence techniques.[19,20]

In recent times, theoretical methods have partly mitigated these limitations by helping in the interpretation of experimental measurements and by making semi-quantitative predictions that have driven experimental efforts in the appropriate direction.[11] First-principles molecular dynamics (MD) methods, for which commercial computational packages are available, are in principle the ideal tools to perform such theoretical studies. For example, by using semiempirical methods to describe the electronic structure, fragmentation of large polymeric molecules has been studied with MD.[21–23] Also combinations of more sophisticated density-functional-theory structural information with MD methods have been recently proposed to reproduce mass spectra[24] and to successfully investigate the fragmentation of small biomolecules in collisions with fast atomic ions (see e.g.[25–34]). However, these methods are extremely expensive and therefore are of no practical use for large systems or for explorative studies that require considering a large variety of initial conditions. In contrast, methods based on statistical mechanics are computationally much more accessible and can thus be very valuable for in situ interpretation of fragmentation experiments[35–42] since quantitative description of the processes can be obtained. Unfortunately, existing computational tools based on statistical methods are usually designed to study a particular type of systems and/or processes, and therefore they do not have the versatility of MD methods.

In this work we present an extension of the statistical Micro-canonical Metropolis Monte Carlo (MMMC) method that goes a step further and can be applied to study fragmentation processes in a large variety of systems irrespective of their composition and the nature of the chemical bonding between their elementary constituents. The proposed extension, which we will call M_3C for short, allows us to investigate fragmentation of systems that range from weakly bound noble-gas clusters to tightly bound carbon clusters and organic molecules. In

its origins, the MMMC method was successfully applied to study thermodynamic properties in nuclear physics,[43] then used to study fragmentation of hot metal clusters[38] and highly excited neutral carbon clusters.[44–46] In essence, the MMMC consists in partitioning the mass, charge, energy, and momentum (linear and angular) of an excited molecular system (which are conserved in the micro-canonical approach) among all accessible fragmentation channels with probabilities governed by considerations of maximum entropy (see Ref.[45]). The key aspect of this methodology is that it provides a random way to move in phase space until a region of maximum entropy is reached, where the physical observables are computed by performing a simple statistical average.

To evaluate fragmentation yields that are directly comparable with experiment, one must know the energy distribution $f(E)$ in the excited/ionized molecular target resulting from the collision with the projectile.[44] However, in most cases, this energy distribution is not known (Refs.[44,47–49] are notable exceptions) and must be estimated from semi empirical arguments or from theoretical simulations performed at different levels of approximation, such as those based on stopping-power methods[50] or on simplified close-coupling approaches.[48,51–54] Conversely, a fit of experimentally determined fragmentation yields to MMMC calculated ones can be used to obtain the unknown energy distribution $f(E)$, which can then be used to interpret other measurements performed under similar experimental conditions. Our new M_3C tool allows one to consider this second approach in a general way.

The paper is organized as follows. First (section 2), we present a detailed theoretical description of the method by considering a molecular system in full generality. We go beyond earlier MMMC derivations[38,45] by formally including the coupling between the angular momenta of the fragments and the energy barriers that may appear on each fragmentation channel. We also present our implementation to compute fragmentation probabilities and species, fragment energy distributions, temperature and heat capacities as a function of the excitation energy, among others. In section 3, we describe the algorithms and strategies used in the M_3C software package based on the above theory. Finally, in section 4, we illustrate

the performance of the method in some prototypical systems. In particular, we evaluate the caloric curve of the weakly bound atomic cluster Ar_{13}, we study the fragmentation of neutral (C_5,C_7,C_9) and singly charged (C_4^+, C_5^+) carbon clusters, and we simulate the mass spectra of the acetylene molecule, C_2H_2. Section (5) summarizes the main conclusions of this work.

2 Theory

In this section we describe in detail the ingredients of our model. As we will show, the main goal is to reach a reliable expression for the *density of states* (DOS) of the system, which is the most important quantity in the microcanonical ensemble. We first present the Metropolis Monte Carlo approximation (section 2.1), where we provide an overview of the method. In the second part (section 2.2) an extended derivation of the DOS is given.

2.1 Microcanonical Metropolis Monte Carlo model

In the definition of the microcanonical ensemble in statistical physics, the system under study (nuclei, atoms, molecules, clusters, spins, etc.) has fixed energy E and its statistical equilibrium is characterized by the microcanonical entropy, which is given by the Boltzmann's formula:

$$\mathcal{S} = k_{\mathrm{B}} \ln \Omega(E) \ , \tag{1}$$

where k_{B} is the Boltzmann's constant and $\Omega(E)$ is the DOS. In the following, in addition to the conservation of energy, we will consider a microcanonical ensemble in which both the total angular momentum $\boldsymbol{\mathcal{J}}_0$ and the total linear momentum $\boldsymbol{\mathcal{P}}_0$ of the system are conserved. Within a semi-classical description, the number of accessible micro-states is proportional to the DOS expressed as:

$$\Omega(E, \boldsymbol{\mathcal{P}}_0, \boldsymbol{\mathcal{J}}_0) = \int d\boldsymbol{\Gamma}\, \delta\Big[\mathcal{H}(\boldsymbol{\Gamma}) - E\Big] \delta\Big[\boldsymbol{\mathcal{J}}(\boldsymbol{\Gamma}) - \boldsymbol{\mathcal{J}}_0\Big] \delta\Big[\boldsymbol{\mathcal{P}}(\boldsymbol{\Gamma}) - \boldsymbol{\mathcal{P}}_0\Big], \tag{2}$$

where $\mathcal{H}(\mathbf{\Gamma})$ represents the Hamiltonian of the system, and $\mathbf{\Gamma}$ the associated phase space (all the possible values of position and momentum coordinates).

We simplify the treatment of the translational motion by referring the linear momentum $\boldsymbol{\mathcal{P}}$ of the constituent fragments to the center-of-mass laboratory-oriented system of coordinates. The constrain in $\boldsymbol{\mathcal{P}}$ can be easily integrated out by fixing $\boldsymbol{\mathcal{P}}_0 = \mathbf{0}$. However, it is not possible to define a system of coordinates where the system does not rotate and, therefore, it is not possible to integrate out the constrain in $\boldsymbol{\mathcal{J}}$ using a similar strategy. However after some approximations, we will show in section 2.2 that Eq. (2) can be approximated as follows

$$\Omega(E, \boldsymbol{\mathcal{J}}_0) \;\approx\; A \sum_{i=1}^{N} \Omega'\left(\boldsymbol{\mathcal{X}}_i; E, \boldsymbol{\mathcal{J}}_0\right) \;, \tag{3}$$

where A is a constant independent of the energy and N is the number of state vectors of a Markov chain in phase space (see below). Therefore, the total DOS may be seen as an average of the *local DOS*, $\Omega'\left(\boldsymbol{\mathcal{X}}; E, \boldsymbol{\mathcal{J}}_0\right)$, which is a function of the system's *state vector*

$$\boldsymbol{\mathcal{X}} = (\mathbf{c}, \mathbf{E}_v, \boldsymbol{\mathcal{R}}, \boldsymbol{\theta}) \;, \tag{4}$$

where $\mathbf{c}$ represents the composition of the system, i.e. the number of fragments (molecules) and their compositions (charge, geometry, electronic configuration, spin multiplicity), $\mathbf{E}_v$ the vibrational energies, $\boldsymbol{\mathcal{R}}$ the positions (cartesian coordinates of the centers of mass of the fragments), and $\boldsymbol{\theta}$ their orientations in space.

The mathematical representation we use for $\Omega'\left(\boldsymbol{\mathcal{X}}; E, \boldsymbol{\mathcal{J}}_0\right)$ is deduced in section 2.2.4; the important point in our approach is to generate the minimum number of state-vectors that provides an accurate description of the DOS according to equation (3). In order to do this, we take advantage of a stochastic sampling method. In particular, we use a Markov chain Monte Carlo sampling algorithm.

The Laplace principle of indifference assigns *a priori* an equal probability to all phase space points situated on the energy surface $\mathcal{H}(\mathbf{\Gamma}) = E$. Therefore, we can write this proba-

bility density as

$$P(\mathbf{\Gamma}; E, \boldsymbol{\mathcal{J}}_0) = \frac{1}{\Omega(E)} \delta\Big[\mathcal{H}(\mathbf{\Gamma}) - E\Big] \delta\Big[\boldsymbol{\mathcal{J}}(\mathbf{\Gamma}) - \boldsymbol{\mathcal{J}}_0\Big] \tag{5}$$

The statistical average of a physical quantity f can be expressed in the space of the system's state-vectors, as follows

$$\Big\langle f \Big\rangle = \int d\mathbf{\Gamma}\ P(\mathbf{\Gamma}) f(\mathbf{\Gamma}) = \sum_{k=1}^{N} P(\boldsymbol{\mathcal{X}}_k) f(\boldsymbol{\mathcal{X}}_k), \tag{6}$$

where we have omitted the parametric dependence on E and $\boldsymbol{\mathcal{J}}_0$ for the sake of simplicity (it will be introduced when needed). Probability density of finding the system in the state $\boldsymbol{\mathcal{X}}_k$ can be written as

$$P(\boldsymbol{\mathcal{X}}_k; E, \boldsymbol{\mathcal{J}}_0) = \frac{\Omega'(\boldsymbol{\mathcal{X}}_k; E, \boldsymbol{\mathcal{J}}_0)}{\Omega(E, \boldsymbol{\mathcal{J}}_0)}. \tag{7}$$

In order to calculate statistical averages, this probability function may be used as a weighting factor in a microcanonical Markov chain Monte Carlo simulation (see e.g.[55–57]). In this method, one moves in small steps (Markov chain)

$$\boldsymbol{\mathcal{X}}_1 \to \boldsymbol{\mathcal{X}}_2 \to \cdots \to \boldsymbol{\mathcal{X}}_k \to \cdots \to \boldsymbol{\mathcal{X}}_N, \tag{8}$$

towards the most important region of the phase space, *i.e.* the region exhibiting the highest values of $\Omega'(\boldsymbol{\mathcal{X}}_k)$, the maximum entropy region. At the k^{th} step, the new generated candidate $\boldsymbol{\mathcal{X}}_{k+1}$ will be accepted or rejected depending on the acceptance ratio $p(\boldsymbol{\mathcal{X}}_k \to \boldsymbol{\mathcal{X}}_{k+1})$, given by

$$p(\boldsymbol{\mathcal{X}}_k \to \boldsymbol{\mathcal{X}}_{k+1}) = \min\left(1, \frac{P(\boldsymbol{\mathcal{X}}_{k+1})}{P(\boldsymbol{\mathcal{X}}_k)}\right) = \min\left(1, \frac{\Omega'(\boldsymbol{\mathcal{X}}_{k+1})}{\Omega'(\boldsymbol{\mathcal{X}}_k)}\right)\ . \tag{9}$$

i.e. the candidate is accepted ($\boldsymbol{\mathcal{X}}_{k+1}$ is used in the next step) if $p \geq 1$, accepted with a finite probability if $\mathcal{U}_{\{0,1\}} \geq p > 1$, or otherwise rejected ($\boldsymbol{\mathcal{X}}_{k+1}$ is discarded and $\boldsymbol{\mathcal{X}}_k$ is reused in the next step). Thus, the Markov chain is given by the accepted state vectors, assuming that, if a point is rejected, the system returns to the previous one ($\mathcal{X}_{k+1} = \mathcal{X}_k$). At the end of the simulation, after equilibration of the system (burn-in period), the expected values of

a quantity f can be approximated by a simple arithmetic average

$$\Big\langle f \Big\rangle = \frac{1}{N}\sum_{k=1}^{N} f(\boldsymbol{\mathcal{X}}_k) \ , \tag{10}$$

where the error on $\langle f \rangle$ scales as $1/\sqrt{N}$, being N the number of state vectors in the Markov chain.

2.2 Computation of the Density of States

We consider a molecule composed of n atoms and that can be fragmented in N_c different ways (channels). The strategy that we use begins with introducing a natural decomposition of the system's phase space, which results from a convenient selection of the interaction potential among the fragments. Therefore, the $(3n \times N_c)-$dimensional problem can be reduced to N_c uncoupled problems (the details are shown in section 2.2.1). Our second approximation is to neglect the ro-vibrational couplings; to this we consider that the system can be treated in the semi-rigid linked atomic framework (section 2.2.2). Consequently, the Hamiltonian model to represent a specific fragmentation channel is separable, which allows one to integrate out the vibrational contribution from the total DOS by convolution. Following a similar strategy to that used in reference,[58] it is possible to integrate out all the linear momenta $\boldsymbol{\mathcal{P}}_\mu$ and the corresponding orbital angular momenta associated to the fragments, $\sum \boldsymbol{\mathcal{R}}_\mu \times \boldsymbol{\mathcal{P}}_\mu$, where all orbital angular momenta collapse to the total orbital angular momentum by taking into account their conservation rules. Finally, by choosing a convenient angular momentum coupling scheme, we reach an expression for the DOS where the angular momentum conservation rules are automatically taken into account (section 2.2.3).

2.2.1 Phase-space channel decomposition

In classical mechanics, the phase space $\mathbf{\Gamma}$ is a $2f$-dimensional space, whose axes are the generalized dynamical coordinates $\mathbf{r}$ and their conjugate momenta $\mathbf{p}$. In this way, each possible state of the system corresponds to one unique point in the phase space. If one considers a system with ν indistinguishable particles and f degrees of freedom, its state is given by the values of $\mathbf{r} = \{r_1, r_2, \cdots, r_f\}$ and $\mathbf{p} = \{p_1, p_2, \cdots, p_f\}$. The integration element in the phase space $\mathbf{\Gamma} = \{\mathbf{r}, \mathbf{p}\}$ reads

$$d^{2f}\mathbf{\Gamma} := \frac{1}{\prod_k \nu_k!} \frac{d^f\mathbf{r}\, d^f\mathbf{p}}{(2\pi\hbar)^f}$$

and it can be considered as the number of quantum states associated with the classical limit within the volume element $d^f\mathbf{r}\, d^f\mathbf{p}$. The first factor at the right hand side of the equation is known as the Gibbs' correction factor, which appears when one takes into account the permutations of different kinds of identical particles.

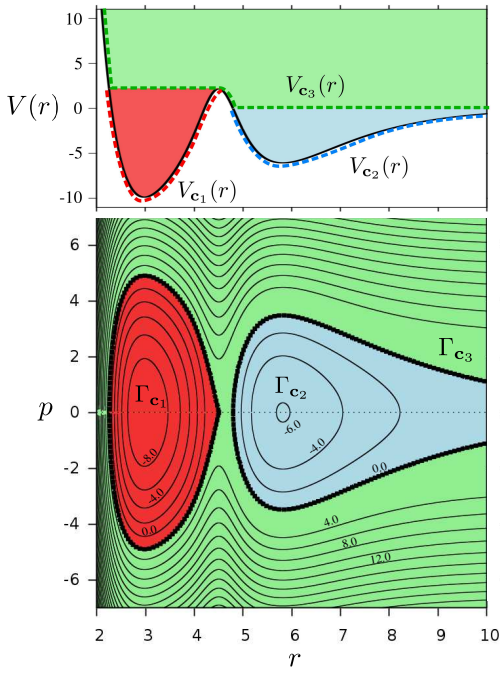

Figure 1: Upper panel: Double well potential for a diatomic hypothetical system AB. Lower panel: Associated phase space and its channel decomposition (see text for details).

Now, in order to introduce the concept of *phase space channel decomposition*, we consider the fragmentation of a diatomic molecule AB, where the interaction between the atoms A and B is given by a double well potential as shown in Fig. 1a. Let us consider the following matrix which represents the composition of the system:

$$\boldsymbol{\mathcal{C}}_{[\mathrm{AB}]} := \begin{array}{c} \\ \mathrm{A} \\ \mathrm{B} \end{array} \begin{array}{c} \begin{array}{cccc} \mathrm{AB} & \mathrm{AB'} & \mathrm{A} & \mathrm{B} \end{array} \\ \begin{pmatrix} 1 & 1 & 1 & 0 \\ 1 & 1 & 0 & 1 \end{pmatrix} \end{array},$$

where the columns are associated to all possible species/fragments (AB, AB', A, and B) and the rows to the atomic constituents of those species/fragments (A and B). Number 1 indicates that a given species or fragment contains a particular atomic constituent, and 0 that it does not. We assign to each species/fragment the set $\mathbf{s}_i = \mathrm{col}_i \boldsymbol{\mathcal{C}}_{[\mathrm{AB}]}$. In this system, there are three possible fragmentation channels: AB($\mathbf{c}_1 = \{\mathbf{s}_1\}$), AB'($\mathbf{c}_2 = \{\mathbf{s}_2\}$) and A+B($\mathbf{c}_3 = \{\mathbf{s}_3, \mathbf{s}_4\}$), where the difference between channels AB and AB' is the internuclear distance. As can be seen, a fragmentation channel is represented as a multiset containing species as elements. At variance with a set, a multiset allows multiple instances of its elements, where the number of instances for a given element is called multiplicity.

After separation of the center-of-mass motion, the associated phase space is the two-dimensional curve plot shown in Fig. 1b. Based on the local maximum position ($r \sim 4.5$Å) and the asymptotic limit of the interaction potential, it is possible to make a partition of the phase space in three regions (see Fig. 1b):

$$\boldsymbol{\Gamma} = \boldsymbol{\Gamma}_{\mathbf{c}_1} \cup \boldsymbol{\Gamma}_{\mathbf{c}_2} \cup \boldsymbol{\Gamma}_{\mathbf{c}_3} \qquad \therefore \qquad \boldsymbol{\Gamma}_{\mathbf{c}_k} \cap \boldsymbol{\Gamma}_{\mathbf{c}_l} = 0, \qquad k \neq l$$

which allows us to define in an univocal way the limits for each fragmentation channel. Consequently, we can associate the points in each region with each channel: $(r,p) \in \boldsymbol{\Gamma}_{\mathbf{c}_1}$ with channel AB, $(r,p) \in \boldsymbol{\Gamma}_{\mathbf{c}_2}$ with channel AB' and $(r,p) \in \boldsymbol{\Gamma}_{\mathbf{c}_3}$ with channel A+B. Therefore,

any kind of integral on the phase space is transformed as follows

$$\int d\mathbf{\Gamma} \quad \Longrightarrow \quad \sum_{j=1}^{3} \int_{\mathbf{\Gamma}_{\mathbf{c}_j}} \frac{d^{f_{\mathbf{c}_j}}\boldsymbol{r}\; d^{f_{\mathbf{c}_j}}\boldsymbol{p}}{(2\pi\hbar)^{f_{\mathbf{c}_j}}} \, .$$

On the other hand, as can be seen in Fig. 1b, the decomposition of the phase space indirectly induces different interaction potentials for each fragmentation channel. Thus we can write three different Hamiltonians associated with each channel

$$\mathcal{H}_{\mathbf{\Gamma}_{\mathbf{c}_j}}(\mathbf{r},\mathbf{p}) = \frac{\mathbf{p}^2}{2m} + U_{\mathbf{c}_j}(\mathbf{r}) \qquad \therefore \qquad j = 1,2,3 \, .$$

It is important to emphasize that this phase space decomposition preserves the Hamiltonian flows, therefore, the ergodicity of the system is also preserved, which is very important in the statistical description that we will use hereafter.

For the general case, the phase space decomposition into N_c fragmentation channels reads as

$$\mathbf{\Gamma} = \bigcup_{j=1}^{N_c} \mathbf{\Gamma}_{\mathbf{c}_j} \qquad \therefore \qquad \mathbf{\Gamma}_{\mathbf{c}_k} \cap \mathbf{\Gamma}_{\mathbf{c}_l} = 0, \qquad k \neq l \, ,$$

and therefore, the integration over the phase space reads

$$\int d\mathbf{\Gamma} \; \Longrightarrow \; \sum_{j=1}^{N_c} \Omega_e(\mathbf{c}_j)\Omega_n(\mathbf{c}_j) \int_{\mathbf{\Gamma}_{\mathbf{c}_j}} \frac{d^{f_{\mathbf{c}_j}}\boldsymbol{r}\; d^{f_{\mathbf{c}_j}}\boldsymbol{p}}{(2\pi\hbar)^{f_{\mathbf{c}_j}}} \, . \tag{11}$$

We have introduced in Eq. (11) the degeneracy of the associated electronic energy level $\Omega_e(\mathbf{c}_j)$ (*i.e.* the electronic DOS) and the combinatorial weight $\Omega_n(\mathbf{c}_j)$ (i.e. the combinatorial DOS) for the channel $\mathbf{c}_j$.

The electronic state degeneracy takes into account the total number of microstates of the electronic states based in the symmetry of the electronic wave function. Explicitly, it is

given by,

$$\Omega_e(\mathbf{c}_j) = \prod_{i=1}^{N_f^{(j)}} \Omega_e(\mathbf{s}_j)$$

$$\Omega_e(\mathbf{s}) = \begin{cases} (2S+1)(2L+1) & \text{if } \mathbf{s} \text{ is an atom} \\ (2S+1) & \text{if } \mathbf{s} \text{ is a linear molecule } (M_L = 0) \\ (2S+1)2|M_L| & \text{if } \mathbf{s} \text{ is a linear molecule } (M_L \neq 0) \\ (2S+1)2D & \text{if } \mathbf{s} \text{ is not a linear molecule} \\ 1 & \text{otherwise.} \end{cases} \tag{12}$$

In the case of atoms, the electronic state degeneracy (assuming LS coupling) is completely specified by the total spin (S) and the total orbital angular momentum (L) quantum numbers. In the case of linear molecules, L is no longer a good quantum number due to lack of spherical symmetry. Thus, the number of micro-states now depend on M_L, which corresponds to the component of L along the molecular axis. Finally, in the case of nonlinear molecules, it is necessary to specify the degeneracy of the associated irreducible representation D, where $D = 1$ for A and B, and $D = 2, 3, 4, 5$ for E, F, G, H, respectively. Notice that by knowing the fragments' atomic/molecular symbol, we can immediately calculate the number of micro-states by using Eq. (12).

The combinatorial weight $\Omega_n(\mathbf{c}_j)$ takes into account that the number of identical particles can change (actually after the phase space decomposition it is necessary to consider *identical fragments* instead of identical particles), keeping invariant the atomic composition and the total charge of the system. It reads

$$\Omega_n(\mathbf{c}_j) = \frac{1}{\prod_k \mathsf{m}\left(\mathbf{s}_k^{(j)}\right)!} \delta\left\{ \sum_{i=1}^{N_f^{(j)}} \mathbf{s}_i^{(j)} - \mathbf{s}_0 \right\} \delta\left\{ \sum_{i=1}^{N_f^{(j)}} z_i^{(j)} - z_0 \right\} \tag{13}$$

where $\mathsf{m}\left(\mathbf{s}_k^{(j)}\right)$ represents the multiplicity of the k-th fragment in the channel $\mathbf{c}_j$, and $\mathbf{s}_0$ and z_0 the identity of the initial fragment and its charge, respectively. Thus, Dirac's delta

functions assure the composition and charge conservation rules. Eq. (13) is a generalization of the weight w_{NZ} (number of ordered partitions of a cluster of N_T atoms and charge Z_T into N_f fragments) defined in our earlier implementation of the MMMC methodology.[45] Indeed, it possible to demonstrate that the weight w_{NZ} is equivalent to the summation of all $\Omega_n(\mathbf{c}_j)$ containing the same number of fragments. However, this description is limited to study molecules with only one kind of atoms. In our new description, Eq. (13) allows us to describe the fragmentation of molecules containing different kinds of atoms.

According to Eq. (11), the integration in phase space can be seen as the summation of the contributions from different independent channels. Thus, in the next section, we focus on obtaining the Hamiltonian function associated to a given channel.

2.2.2 Hamiltonian Model for a Fragmentation Channel

In our model we consider three approximations: (i) we assume the validity of the Born-Oppenheimer approximation, (ii) a given fragmentation channel is represented as a set of molecules/fragments constructed in a semi-rigidly linked atomic framework, where the interaction between them are introduced by a pair-wise like potential that depends on the distance between their centers of mass and does not consider their relative orientations; (3) we consider a harmonic expansion for the internal degrees of freedom for each fragment ($\mathbf{Q}$,$\mathbf{P}$).

If one denotes by $\boldsymbol{\mathcal{R}} = \left\{\boldsymbol{\mathcal{R}}_1, \boldsymbol{\mathcal{R}}_2, \ldots, \boldsymbol{\mathcal{R}}_{N_f}\right\}$ the center-of-mass positions of all the fragments with respect to the laboratory frame (lab), $\boldsymbol{\theta} = \left\{\boldsymbol{\theta}_1, \boldsymbol{\theta}_2, \ldots, \boldsymbol{\theta}_{N_f}\right\}$ their orientations with respect to their own body-fix frame (bf), where $\boldsymbol{\theta} = (\alpha, \beta, \gamma)$ represents the Euler angles ($\mathbb{R}(\boldsymbol{\theta})$ is the associated rotation matrix that allows to convert from $lab \rightarrow bf$) and $\mathbf{Q} = \left\{\mathbf{Q}_1, \mathbf{Q}_2, \ldots, \mathbf{Q}_{N_f}\right\}$ their internal atomic displacements in mass-weighted coordinates around their equilibrium geometries (vibrations), it is possible to show that the classical

Hamiltonian for a given fragmentation channel is given by (see e.g.[59–61]):

$$\mathscr{H}(\boldsymbol{\mathcal{R}},\boldsymbol{\mathcal{P}},\boldsymbol{\theta},\mathbf{J},\mathbf{Q},\mathbf{P}) = \sum_{\mu=1}^{N_f}\left\{\frac{1}{2}\boldsymbol{\mathcal{P}}_\mu^{\mathrm{T}}\mathbf{M}_\mu^{-1}\boldsymbol{\mathcal{P}}_\mu + \frac{1}{2}\mathbf{J}_\mu^{\mathrm{T}}\mathbf{I}_\mu^{-1}\mathbf{J}_\mu + \frac{1}{2}\mathbf{P}_\mu^{\mathrm{T}}\mathbf{P}_\mu + \frac{1}{2}\mathbf{Q}_\mu^{\mathrm{T}}\boldsymbol{f}_\mu\mathbf{Q}_\mu\right\} + U(\boldsymbol{\mathcal{R}}) \quad (14)$$

where $\boldsymbol{\mathcal{P}}$ and $\mathbf{P}$ are the canonical conjugate momenta of $\boldsymbol{\mathcal{R}}$ and $\mathbf{Q}$ respectively, $\mathbf{M}_\mu$ is a 3×3 matrix associated with the mass of the fragments $\mathbf{M}_\mu = m_\mu\mathbf{I}_{3\times3}$, and $\mathbf{f}_\mu$ represents the force constant matrix

$$\{\mathbf{f}_\mu\}_{ij} = \frac{1}{\sqrt{m_{i\mu}m_{j\mu}}}\left(\frac{\partial^2 U}{\partial x_{i\mu}\partial x_{j\mu}}\right), \quad (15)$$

which can be diagonalized in order to obtain the $f_{v\mu}$ vibrational frequencies associated to each fragment $\boldsymbol{\omega}_\mu = \{\omega_{1\mu},\omega_{2\mu},\ldots,\omega_{f_{v\mu}\mu}\}$. $\mathbf{I}_\mu$ is the inertia tensor related to the rotation of the μ-th fragment around its center-of-mass, in the body-fix frame of reference with an angular momentum $\mathbf{J}_\mu$.

The potential energy in our Hamiltonian model, $U(\boldsymbol{\mathcal{R}})$, as we said above, is defined as the sum of the pairwise interactions between the fragments given by

$$U(\boldsymbol{\mathcal{R}}) \approx \sum_{\mu=1}^{N_f} U_\mu^{(1)} + \sum_{\mu=1}^{N_f-1}\sum_{\nu=\mu}^{N_f} U_{\mu\nu}^{(2)}(|\boldsymbol{\mathcal{R}}_{\mu\nu}|)\ , \quad (16)$$

where $U_\mu^{(1)}$ is the one-body contribution of the μ-th fragment (equivalent to electronic energy) and $U_{\mu\nu}^{(2)}(|\boldsymbol{\mathcal{R}}_{\mu\nu}|)$ is the two-body energy term which depends on the distance between the two fragments μ and ν, and that goes to zero as $|\boldsymbol{\mathcal{R}}_{\mu\nu}| \equiv |\boldsymbol{\mathcal{R}}_\mu - \boldsymbol{\mathcal{R}}_\nu|$ tends to infinity. This strategy provides a way to calculate the total interacting potential once all the pairwise interactions between the fragments are obtained.

2.2.3 Density of States for a Fragmentation Channel

After the definition of the Hamiltonian, we perform a few algebraic transformations in order to obtain an expression for the DOS of the system that is easily integrable. In particular, we show the factorization of the DOS in their vibrational, rotational and translational components. The factorization of the last component involves an integration in the configurational

space that will be approximated by a Monte Carlo scheme in section 2.2.4.

By using the "phase space channels decomposition" of Eq. (11) in the definition of the DOS [see Eq. (2)], we obtain

$$\Omega(E) = \sum_{j=1}^{N_c} \Omega_e(\mathbf{c}_j)\Omega_n(\mathbf{c}_j)\Omega_{\mathbf{c}_j}(E) \tag{17}$$

Thus, the DOS is now decomposed into several components, each one associated to one channel. In the above expression, we have introduced the *DOS for the* $\mathbf{c}_j$ *channel*, $\Omega_{\mathbf{c}_j}(E)$, which can be explicitly written in the system of coordinates defined in the previous subsection as follows,

$$\Omega_{\mathbf{c}}(E) = \int \frac{d^{3N_f}\boldsymbol{\mathcal{R}}\; d^{3N_f}\boldsymbol{\mathcal{P}}}{(2\pi\hbar)^{3N_f}}\; \frac{d^{f_r}\boldsymbol{\theta} d^{f_r}\mathbf{J}}{(2\pi\hbar)^{f_r}}\; \frac{d^{f_v}\mathbf{Q} d^{f_v}\mathbf{P}}{(2\pi\hbar)^{f_v}} \times \delta\Big[\mathscr{H}(\boldsymbol{\mathcal{R}},\boldsymbol{\mathcal{P}},\boldsymbol{\theta},\mathbf{J},\mathbf{Q},\mathbf{P}) - E\Big]\delta\Big[\boldsymbol{\mathcal{J}} - \boldsymbol{\mathcal{J}}_0\Big]\delta\Big[\boldsymbol{\mathcal{P}} - \boldsymbol{\mathcal{P}}_0\Big] \tag{18}$$

$$d^f\mathbf{X} = \prod_{\mu=1}^{N_f} d^{f_\mu}\boldsymbol{X}_\mu \quad \therefore \quad \mathbf{X} = \boldsymbol{\mathcal{R}},\boldsymbol{\mathcal{P}},\mathbf{J},\mathbf{Q},\mathbf{P}, \qquad d^{f_r}\boldsymbol{\theta} = \prod_{\mu=1}^{N_f} \frac{1}{\sigma_\mu}\sin\beta_\mu\; d^{f_{r\mu}}\boldsymbol{\theta}_\mu$$

where, for simplicity, we have omitted the DOS dependence with the identity of the channel (it will be introduced when needed). f_r is the number of rotational degrees of freedom $f_r = \sum_\mu f_{r\mu}$ and f_v is the number of vibrational degrees of freedom $f_v = \sum_\mu f_{v\mu}$. Notice that $\mathbf{J}$ is not the canonical conjugate momenta of $\boldsymbol{\theta}$. This is the origin of the prefactor $\sin\beta_\mu$ which is the Jacobian of the associated transformation. σ_μ is the rotational symmetry number, it indicates the number of unique orientations of the μ-th fragment that only interchange

identical atoms. This number depends on the fragment's molecular symmetry

$$\sigma_\mu = \begin{cases} 1 & \text{if} \quad \mu \in C_1, C_i, C_s, C_{\infty v} \\ 2 & \text{if} \quad \mu \in D_{\infty h} \\ n & \text{if} \quad \mu \in C_n, C_{nv}, C_{nh} \\ 2n & \text{if} \quad \mu \in D_n, D_{nh}, D_{nd} \\ n/2 & \text{if} \quad \mu \in S_n \end{cases} \tag{19}$$

The Hamiltonian function is separable since rotational-vibrational couplings have been ignored; therefore, it is possible to use the convolution theorem to separate the vibrational contribution from the rest of degrees of freedom as follows

$$\Omega_{\mathbf{c}}(E) = \int_0^E \Omega_v(\mathbf{c}, E_v)\Lambda(\mathbf{c}, E - E_v)\ dE_v \tag{20}$$

where $\Omega_v(\mathbf{c}, E_v)$ is the *vibrational DOS* associated to the channel $\mathbf{c}$ and is given by

$$\Omega_v(\mathbf{c}, E_v) = \int \frac{d^{f_v}\mathbf{Q} d^{f_v}\mathbf{P}}{(2\pi\hbar)^{f_v}}\ \delta\left[\sum_{\mu=1}^{N_f} \left\{ \frac{1}{2}\mathbf{P}_\mu^{\mathrm{T}}\mathbf{P}_\mu + \frac{1}{2}\mathbf{Q}_\mu^{\mathrm{T}}\boldsymbol{\omega}_\mu^2\mathbf{Q}_\mu \right\} - E_v \right]. \tag{21}$$

This equation corresponds to the DOS for a set of f_v uncoupled harmonic oscillators grouped in N_f sets (one for each fragment). By using the convolution theorem N_f times, we integrate out the contribution of the vibrational DOS for each fragment which admits the following solution

$$\Omega_{\mathbf{c}}(E) = \int \prod_{\mu=1}^{N_f} dE_{v\mu}\ \ \Omega_{v\mu}(\mathbf{c}, E_{\nu\mu})\Lambda(\mathbf{c}, E - E_v), \qquad \Omega_{v\mu}(\mathbf{c}, E) = \frac{E^{f_{v\mu}-1}}{\hbar^{f_{v\mu}}\Gamma\left(f_{v\mu}\right)} \prod_{k=1}^{f_{v\mu}} \omega_{\mu k}^{-1}\ . \tag{22}$$

The total vibrational energy should satisfy the constraint $E_v = \sum_{\mu=1}^{N_f} E_{v\mu}$, being $E_{v\mu}$ the vibrational energy of the μ-fragment, with $f_{v\mu}$ internal vibrational degrees of freedom, and $\omega_{\mu 1}, \omega_{\mu 2}, \ldots, \omega_{\mu f_{v\mu}}$ the associated vibrational frequencies. As in previous work,[45] we

suppose that the maximum energy that a fragment can absorb is limited by the lowest dissociation energy $D_{e\mu}$, i.e., the vibrational energy for the μ-fragment is constrained to satisfy $0 \leq E_{v\mu} \leq D_{e\mu}$. $\Lambda(\mathbf{c}, E)$ involves the rest of the degrees of freedom (rotation and translation of the fragments in the channel):

$$\Lambda(\mathbf{c}, E) = \int \frac{d^{3N_f}\boldsymbol{\mathcal{R}}\; d^{3N_f}\boldsymbol{\mathcal{P}}}{(2\pi\hbar)^{3N_f}} \; \frac{d^{f_r}\boldsymbol{\theta} d^{f_r}\mathbf{J}}{(2\pi\hbar)^{f_r}} \times\delta\left[\sum_{\mu=1}^{N_f} \frac{1}{2}\boldsymbol{\mathcal{P}}_\mu^{\mathrm{T}}\mathbf{M}_\mu^{-1}\boldsymbol{\mathcal{P}}_\mu + \sum_{\mu=1}^{N_f} \frac{1}{2}\mathbf{J}_\mu^{\mathrm{T}}\mathbf{I}_\mu^{-1}\mathbf{J}_\mu + U(\boldsymbol{\mathcal{R}}) - E \right] \times\delta\big[\boldsymbol{\mathcal{J}} - \boldsymbol{\mathcal{J}}_0\big]\delta\big[\boldsymbol{\mathcal{P}} - \boldsymbol{\mathcal{P}}_0\big] \; . \tag{23}$$

This equation is particularly hard to solve due to the complexity in treating the coupling of the angular momentum with the orbital rotation of the fragments, induced by the total angular momentum conservation rule. In order to integrate it, we follow a similar strategy as the one proposed in refs.[62–66] We first fix the coordinate variables $\boldsymbol{\mathcal{R}}$ and $\boldsymbol{\theta}$, and then we integrate over the momentum variables $\boldsymbol{\mathcal{P}}$ and $\boldsymbol{J}$. Finally we integrate over $\boldsymbol{\mathcal{R}}$ and $\boldsymbol{\theta}$.

Firstly, to eliminate the translational motion $\boldsymbol{\mathcal{P}}$ we refer the coordinates $\boldsymbol{\mathcal{R}}_\mu$ and their conjugate momenta $\boldsymbol{\mathcal{P}}_\mu$ of the fragments to the center of mass laboratory system of coordinates ($\boldsymbol{\mathcal{P}}_0 = \mathbf{0}$). In contrast with $\boldsymbol{\mathcal{P}}$, it is impossible to define a system of reference where the system does not rotate, then it is not possible to integrate out the rotational motion $\boldsymbol{\mathcal{J}}$ from Eq. (23).

To overcome this problem, we can picture the evolution of the overall rotation of a nonrigid system as a rotational motion of a changing rigid body, as it was previously used by Jellinek and Ly[58] in the case of rotating floppy systems like argon clusters. To this, we define $\boldsymbol{\mathcal{P}}_\mu^{\mathrm{rb}}$ as the momenta of the fragments composing the ideal rigid body system. Then, using $\Delta\boldsymbol{\mathcal{P}}_\mu = \boldsymbol{\mathcal{P}}_\mu - \boldsymbol{\mathcal{P}}_\mu^{\mathrm{rb}}$, the constraint in the total angular momentum and the kinetic energy is

transformed as follow (see details in[58])

$$\begin{aligned}\boldsymbol{\mathcal{J}}-\boldsymbol{\mathcal{J}}_0 &\longrightarrow \boldsymbol{L}+\sum_{\mu=1}^{N_f}\mathbb{R}(\boldsymbol{\theta})_\mu^T\boldsymbol{J}_\mu-\boldsymbol{\mathcal{J}}_0\\ \sum_{\mu=1}^{N_f}\frac{1}{2}\boldsymbol{\mathcal{P}}_\mu^{\mathrm{T}}\mathrm{M}_\mu^{-1}\boldsymbol{\mathcal{P}}_\mu &\longrightarrow \sum_{\mu=1}^{N_f}\frac{1}{2}\boldsymbol{\Delta\mathcal{P}}_\mu^{\mathrm{T}}\mathrm{M}_\mu^{-1}\boldsymbol{\Delta\mathcal{P}}_\mu+\frac{1}{2}\boldsymbol{L}^T\boldsymbol{\mathcal{I}}^{-1}\boldsymbol{L},\end{aligned} \tag{24}$$

where the total orbital angular momentum is defined by $\boldsymbol{L}=\sum_\mu \boldsymbol{\mathcal{R}}_\mu\times\boldsymbol{\mathcal{P}}_\mu^{\mathrm{rb}}$, and $\boldsymbol{\mathcal{I}}^{-1}$ represents the associated tensors of inertia for the overall rotation of the system as a rigid body. This approximation introduces a complete instantaneous decoupling of the overall rotation energy ($\boldsymbol{L}^T\boldsymbol{\mathcal{I}}^{-1}\boldsymbol{L}/2$) from those fragments' relative motions, giving zero Coriolis contribution in the Hamiltonian. Note that since the tensor of inertia $\boldsymbol{\mathcal{I}}^{-1}$ depends on the instantaneous fragments' position, the dynamical coupling in the system is fully retained and the overall rotation and the internal displacements exchange energy. Replacing (24) in (23) we obtain,

$$\begin{aligned}\Lambda(\mathbf{c},E)=\int \frac{d^{3N_f}\boldsymbol{\mathcal{R}}\,d^{3N_f}\boldsymbol{\Delta\mathcal{P}}}{(2\pi\hbar)^{3N_f}}\,\frac{d^{f_r}\boldsymbol{\theta}d^{f_r}\mathbf{J}}{(2\pi\hbar)^{f_r}}\\ \times\delta\left[\sum_{\mu=1}^{N_f}\frac{1}{2}\boldsymbol{\Delta\mathcal{P}}_\mu^{\mathrm{T}}\mathrm{M}_\mu^{-1}\boldsymbol{\Delta\mathcal{P}}_\mu+E_{\mathrm{rot}}(\mathbf{J},\boldsymbol{L};\boldsymbol{\mathcal{R}})+U(\boldsymbol{\mathcal{R}})-E\right]\\ \times\delta\left[\boldsymbol{L}+\sum_{\mu=1}^{N_f}\mathbb{R}(\boldsymbol{\theta})_\mu^T\boldsymbol{J}_\mu-\boldsymbol{\mathcal{J}}_0\right],\end{aligned} \tag{25}$$

where the rotational energy is given by:

$$E_{\mathrm{rot}}(\mathbf{J},\boldsymbol{L};\boldsymbol{\mathcal{R}})=\frac{1}{2}\sum_\mu \boldsymbol{J}_\mu^T\boldsymbol{I}_\mu^{-1}\boldsymbol{J}_\mu+\frac{1}{2}\boldsymbol{L}^T\boldsymbol{\mathcal{I}}^{-1}(\boldsymbol{\mathcal{R}})\boldsymbol{L} \tag{26}$$

The usual strategy to solve equations like (25) is to reduce the argument of the first delta function to a diagonal quadratic form. In this case we just simply transform $\boldsymbol{\Delta\mathcal{P}}$ into a Jacobi system of coordinates (see for example[45]). However, in the rotational energy term, the angular momentum constraint prevents this possibility for the $\mathbf{J}$ coordinates. So, we

have to find a transformation of $\mathbf{J}$ where the rotational energy is formally diagonalized.

The strategy we use starts by substituting $\boldsymbol{L}$ from the angular momentum constrain in Eq. (25) into Eq. (26). Then the rotational energy can be rewritten as,

$$\begin{aligned} E_{\text{rot}}(\boldsymbol{J};\boldsymbol{\mathcal{R}},\boldsymbol{\theta}) &= \frac{1}{2}\sum_{\mu=1}^{N_f}\sum_{\nu=1}^{N_f}\mathbf{J}_\mu^T\mathbb{I}_{\mu\nu}^{-1}(\boldsymbol{\theta},\boldsymbol{\mathcal{R}})\mathbf{J}_\nu + E_{\mathcal{J}_0}(\boldsymbol{\mathcal{R}}) \\ \mathbb{I}_{\mu\nu}^{-1}(\boldsymbol{\theta},\boldsymbol{\mathcal{R}}) &:= \mathbf{I}_\mu^{-1} + \mathbb{R}_\mu(\boldsymbol{\theta})\boldsymbol{\mathcal{I}}^{-1}(\boldsymbol{\mathcal{R}})\mathbb{R}_\nu^T(\boldsymbol{\theta}) \\ E_{\mathcal{J}_0}(\boldsymbol{\mathcal{R}}) &:= \frac{1}{2}\boldsymbol{\mathcal{J}}_0^T\boldsymbol{\mathcal{I}}^{-1}(\boldsymbol{\mathcal{R}})\boldsymbol{\mathcal{J}}_0 \end{aligned} \tag{27}$$

where we have introduced the energy associated to the overall rotation $E_{\mathcal{J}_0}$ and the coupling terms $\mathbb{I}_{\mu\nu}^{-1}$. The diagonal elements $\mathbb{I}_{\mu\mu}^{-1}$ play the role of effective inertia tensors for the μ-th fragment and the off-diagonal terms represent the strength of the interaction among angular momenta of different fragments. In our previous implementation,[45] off-diagonal terms and overall rotation were not taken into account.

To obtain Eq. (27), we have omitted the coupling terms $\boldsymbol{J}_\mu^T\boldsymbol{\mathcal{J}}_0$. Note that the angular momentum conservation holds when all these coupling terms are kept. However, to keep the advantage of a fast numerical scheme, we have omitted such terms. These terms allow exchange of energy between rotation of the fragments and the overall rotation of the system, which is less important than the direct coupling between fragments ($\boldsymbol{J}_\mu^T\boldsymbol{J}_\nu$) and the centrifugal distortion ($\boldsymbol{\mathcal{J}}_0^T\boldsymbol{\mathcal{J}}_0$). For low values of $\boldsymbol{\mathcal{J}}_0$, this approximation does not compromise the accuracy of the solution.

Then, by diagonalization of the $\mathbb{I}^{-1} = \{\mathbb{I}_{\mu\nu}^{-1}\}$ matrix, we reach our aim. Indeed, if we denotate by $\mathbf{B}^{-1}$ the diagonal representation of $\mathbb{I}^{-1}$ (*i.e.* $\mathbb{I}^{-1} = \mathbf{U}\mathbf{B}^{-1}\mathbf{U}^T$), the rotational energy gets the expected quadratic form in the new basis of angular momentum vectors $\mathbf{j}$ (where $\mathbf{j} = \mathbf{U}^T(\mathbf{J}_1|\mathbf{J}_2|\cdots|\mathbf{J}_{N_f})^T$ being $\mathbf{U}$ an unitary matrix),

$$E_{\text{rot}}(\mathbf{j};\boldsymbol{\mathcal{R}},\boldsymbol{\theta}) = \frac{1}{2}\mathbf{j}^T\mathbf{B}^{-1}(\boldsymbol{\mathcal{R}},\boldsymbol{\theta})\mathbf{j} + E_{\mathcal{J}_0}(\boldsymbol{\mathcal{R}}) \tag{28}$$

Thus, the new angular momenta $\mathbf{j}$ provide a basis where the contributions to the internal

rotational energy are formally diagonalized. The angular momenta $\mathbf{j}$ can then be calculated from Eq. (28), although it is not straightforward to recover the contribution from each individual fragment, since this information is lost in the diagonalization of $\mathbb{I}^{-1}$. In any case, these individual contributions are not relevant for the DOS, because the final expression does not include them.

Finally, after performing the transformations outlined above, the term in the first Dirac's delta function of Eq. (25) is now diagonal and can be integrated out by using a special case of the Dirichlet equation (see for example[67,68]). This case corresponds to the surface of the s-dimensional hyper-ellipsoid, being s the total number of degrees of freedom (*i.e.* $s = f_t + f_r$). We get:

$$\Lambda(\mathbf{c}, E) = \frac{(2\pi)^{s/2}}{\Gamma(s/2)} \left(\frac{1}{M} \prod_{\mu=1}^{N_f} m_\mu \right)^{3/2} \int \frac{d^{f_t}\boldsymbol{\mathcal{R}}}{(2\pi\hbar)^{f_t}} \frac{d^{f_r}\boldsymbol{\theta}}{(2\pi\hbar)^{f_r}} \times \det \mathbf{B}(\boldsymbol{\mathcal{R}}, \boldsymbol{\theta})^{1/2} \left[E - U(\boldsymbol{\mathcal{R}}) - E_{\mathcal{J}_0}(\boldsymbol{\mathcal{R}}) \right]^{s/2-1} \tag{29}$$

Notice that the term involving the fragments' mass (m_μ) and the total mass of the system ($M = \sum_\mu m_\mu$) is obtained by integration of the linear momenta; in contrast the matrix $\mathbf{B}$ is produced from the integration of the angular momenta. Equation (29) is general and encompasses equations previously developed by other authors for particular cases. For example, in refs.,[63,64] analytical expressions for up to 3 particles were obtained by including the internal rotations as orbital angular momentum contributions. If angular momentum contributions ($\mathbf{J}_\mu$) are ignored in Eq. (29) and orbital angular momentum components ($\boldsymbol{\mathcal{R}}_\mu \times \boldsymbol{\mathcal{P}}_\mu$) are removed from their description, one gets an equivalent formulation. By ignoring the total angular momenta contribution, i.e., the off-diagonal coupling terms $\mathbf{J}_\mu^T \mathbf{J}_\nu$, and by replacing the rotational matrices by unitary matrices, we recover the expression used in our previous implementation.[45] When only atomic fragments are considered, we recover an almost similar expression as that obtained by Calvo and Labastie.[65] In the case of two asymmetric top

interacting fragments, we retrive the equation proposed by Smith in Ref.[69]

2.2.4 Monte Carlo Integration

The last step in our derivation of the DOS is the integration in configurational space as given in Eq. (29) and the convolution defined in Eq. (22). Due to the complexity of these integrals, we adopt a simple Monte-Carlo description by performing a random-sampling of the positions and relative orientations of the fragments ($\boldsymbol{\mathcal{R}}$ and $\boldsymbol{\theta}$) in Eq. (29) and a random-sampling of the fragments' vibrational energy ($E_{\nu\mu}$) in Eq. (22).

To obtain an expression for the first integral, we generate $\mathcal{N}$ configurations, randomly distributed throughout the domain of $\boldsymbol{\mathcal{R}}$ and $\boldsymbol{\theta}$. Hence, the approximation to the integral in Eq. (29) is simply

$$\Lambda(\mathbf{c}, E) \approx \frac{1}{\mathcal{N}} V_{\mathcal{R}} V_{\boldsymbol{\theta}} \sum_{k=1}^{\mathcal{N}} \overline{\Lambda}\big(\mathbf{c}, E, \boldsymbol{\mathcal{R}}_k, \boldsymbol{\theta}_k\big) \tag{30}$$

where we introduced the volume elements associated to the configurational space ($V_{\boldsymbol{\mathcal{R}}}$ and $V_{\boldsymbol{\theta}}$) and the function $\overline{\Lambda}\big(\mathbf{c}, E, \boldsymbol{\mathcal{R}}, \boldsymbol{\theta}\big)$, which gives the contribution of the translational and rotational DOS,

$$\overline{\Lambda}\big(\mathbf{c}, E, \boldsymbol{\mathcal{R}}, \boldsymbol{\theta}\big) = \frac{(2\pi)^{s/2}}{\Gamma(s/2)} \left(\frac{1}{M} \prod_{\mu=1}^{N_f} m_\mu \right)^{3/2} \det \mathbf{B}(\boldsymbol{\theta})^{1/2} \Big[E - U(\boldsymbol{\mathcal{R}}) - E_{\mathcal{J}_0}(\boldsymbol{\mathcal{R}}) \Big]^{s/2-1} . \tag{31}$$

The *configurational free volume* is:

$$V_{\boldsymbol{\mathcal{R}}} = \int \frac{d^{f_t}\boldsymbol{\mathcal{R}}}{(2\pi\hbar)^{f_t}} \quad \therefore \quad |\boldsymbol{\mathcal{R}}_\mu - \boldsymbol{\mathcal{R}}_\nu| > \gamma_\mu + \gamma_\nu \tag{32}$$

To compute it we considered N random configurations in the f_t-dimensional space. Around each atom of each fragment, we build a small imaginary hard sphere of radius r (covalence radius). The volume defined by these spheres is forbidden to occupation by any of the other fragments. Then, the calculation of $V_{\boldsymbol{\mathcal{R}}}$ consists in computing the total number of non-self overlapping configurations among the N steps. The exact solution for this problem

has only been found in one dimension. There are, however, several methods available for computing an approximate solution. We use here the same method described in our previous implementation.[45] The *angular volume* is given by,

$$V_{\boldsymbol{\theta}} = \int \prod_{\mu=1}^{N_f} \left[\frac{1}{\sigma_\mu} \sin\beta_\mu \; \frac{d^{f_{r\mu}}\boldsymbol{\theta}_\mu}{(2\pi\hbar)^{f_{r\mu}}} \right] \tag{33}$$

This factor appears due to the angular part of the eigenrotation of the fragments, and it depends on the symmetry of each molecule. We can distinguish three cases as a function of the number of rotational degrees of freedom: single atoms ($f_{r\mu} = 0$), linear molecular fragments ($f_{r\mu} = 2$) and non-linear molecular fragments ($f_{r\mu} = 3$). Its solution is analytic and corresponds to the surface of a $(f_{r\mu}+1)$-dimensional sphere. Thus it is simply given by:

$$V_{\boldsymbol{\theta}} = \prod_{\mu=1}^{N_f} \frac{1}{\sigma_\mu (2\pi\hbar)^{f_{r\mu}}} \begin{cases} 8\pi^2 & \text{if} \quad f_{r\mu} = 3 \\ 4\pi & \text{if} \quad f_{r\mu} = 2 \\ 1 & \text{otherwise.} \end{cases} \tag{34}$$

To obtain an expression for the convolution integral in Eq. (22), we randomly generate $\mathcal{N}_v$ values of vibrational energy distributed among all fragments. Then, Eq. (22) can be approximated by,

$$\Omega_{\mathbf{c}}(E) \approx A \sum_{j=1}^{N_v} \Omega_v(\mathbf{c}, E_{v,j}) \Lambda(\mathbf{c}, E - E_{v,j}), \tag{35}$$

being A a constant. And finally, by replacing Eq. (30) and Eq. (35) in Eq. (17) we obtain an accessible expression to the DOS of the system, which reads,

$$\begin{gathered} \Omega(E) \approx A \sum_{i=1}^{N_c} \sum_{j=1}^{N_v} \sum_{k=1}^{\mathcal{N}} \; \Omega\left(E, \mathbf{c}_i, E_{v,j}, \boldsymbol{\mathcal{R}}_k, \boldsymbol{\theta}_k\right) \\ \Omega\left(E, \mathbf{c}, E_{v,j}, \boldsymbol{\mathcal{R}}, \boldsymbol{\theta}\right) := \Omega_n(\mathbf{c}) \; \Omega_e(\mathbf{c}) \; \Omega_v\big(\mathbf{c}, E_{v,j}\big) \; V_{\boldsymbol{\mathcal{R}}} \; V_{\boldsymbol{\theta}} \; \overline{\Lambda}\big(\mathbf{c}, E - E_v; \boldsymbol{\mathcal{R}}, \boldsymbol{\theta}\big). \end{gathered} \tag{36}$$

Eq. (36) gives the total DOS as an overall sum, which is carried out over N_c random trials of the available fragmentation channels $\mathbf{c}$, N_v random trials of their vibrational energies $\mathbf{E}_v$, and $\mathcal{N}$ random trials of their positions $\boldsymbol{\mathcal{R}}$ and orientations $\boldsymbol{\theta}$. These trials are always carried out ensuring conservation of the total energy:

$$E = K + \sum_{\mu} E_{v\mu} + U(\boldsymbol{\mathcal{R}}) + E_{\mathcal{J}_0} \tag{37}$$

We take advantage of defining the state of the system as a vector $\boldsymbol{\mathcal{X}}$ that contains independent variables (called the *state vector* of the system):

$$\boldsymbol{\mathcal{X}} = (\mathbf{c}, \mathbf{E}_v, \boldsymbol{\mathcal{R}}, \boldsymbol{\theta}, \mathbf{J}), \tag{38}$$

which allows us to represent the DOS as a simple average by considering N random state-vectors (see equation (3)).

3 Overview of the M_3C program

M_3C is a general-purpose code, though it primary targets are those fragmentation processes that take place through non-radiative transitions, where their fragments remain together enough time such that the excess of energy becomes randomly distributed over all internal degrees of freedom. As a general-purpose code, M_3C is highly customizable and includes many features. Here we briefly describe some of them. The package is divided into three parts:

In the first part, M_3C is able to obtain data from electronic structure calculations by interfacing with some standard quantum chemistry programs. The simplest systems require quantities such as geometries, electronic energies and harmonic frequencies for each molecule to be considered. However, it is also possible to include analytical intermolecular potential energy curves in order to describe weakly bounded systems or special effects like Coulomb

repulsion in fragmentation of multiply charged molecules. In this part, cartesian coordinates and vibrational frequencies results are stored in external files in one of the two most popular formats (XYZ or MOLDEN).[70] These formats are used for many different electronic calculation programs. Currently M_3C offers some bash scripts, to be used as interfaces with GAMESS[71,72] and GAUSSIAN[73] that allow for a stochastic search for isomers. Each step involves a geometry optimization, where the initial geometry is provided by the M_3C algorithm that samples the configurational space. Duplicate isomers are automatically removed. It is possible to discard some chemical species in advance based on stability arguments or based on the peaks which appear in the experimental mass spectra, if available. This could be very important for molecular systems that contain a large number of particles (fragments), since the search for isomers is the most expensive computational part of this methodology. This step provides the so called fragmentation model, which is analyzed in section (3.1).

The second part of the package performs the calculation of the statistical model itself. This part is not self-sufficient, since it requires the molecular properties of the fragments, usually provided after the first part has been performed. One important feature of the code is that it uses a very convenient way to define the Markov-Chain, as described in section (3.2). The program manages several numerical experiments, where each one differs from each other in their initial state-vectors, which are randomly chosen. At the end of the calculation, all observables are reported with their errors estimated from the replica's standard deviation, which may be used as a convergence criteria. The user controls in the input file the maximum permissible error in the standard deviation of the observables by specifying the number of steps in the Markov-Chain, the number of numerical experiments and the burn-in period. Tipically $\sim$50000 steps, 4 numerical experiments and 10% of burn-in period are enough to reach errors lower than 10%.

The third part includes a set of tools which allows the user to analyze the obtained results with a graphical interface, as gnuplot.[74] Some available features that can be calculated are: probability density distributions for channels or fragments as a function of the internal

energy, fragmentation branching ratios based on a given or a fitted deposited energy function, coincidence patterns between several pairs of energy components for a given internal energy, among others.

3.1 Setting up a Fragmentation Model

A fragmentation model consists of a set containing all possible chemical species that may play some role during the fragmentation process, including possible isomers. In order to illustrate this, let us consider the particular case of the CH_2 molecule. This molecule can break leading to different fragments (or *species*):

$$\mathbf{S} = \{\mathrm{CH_2},\ \mathrm{CH},\ \mathrm{H_2},\ \mathrm{H},\ \mathrm{C}\} \tag{39}$$

Each one of these *species* can be characterized by several electronic states or geometries, which we will call *isomers*:

$$\begin{aligned}
\mathrm{CH_2} &= \left\{\ \mathrm{CH_2(X\,^3B_1)},\ \mathrm{CH_2(a\,^1A_1)},\ \cdots\ \right\} \\
\mathrm{CH} &= \left\{\ \mathrm{CH(X\,^2\Pi)},\ \mathrm{CH}(a\,^4\Sigma^-),\ \cdots\ \right\} \\
\mathrm{H_2} &= \left\{\ \mathrm{H_2(X\,^1\Sigma_g^+)},\ \mathrm{H_2}(a\,^3\Sigma_u^+),\ \cdots\ \right\} \\
\mathrm{H} &= \left\{\ \mathrm{H}(\,^2S),\ \mathrm{H}(\,^2P),\ \cdots\ \right\} \\
\mathrm{C} &= \left\{\ \mathrm{C}(\,^3P),\ \mathrm{C}(\,^1D),\ \cdots\ \right\}
\end{aligned} \tag{40}$$

On the other hand, the molecule can experience different *fragmentation reactions*,

$$\mathbf{R} = \{\mathrm{CH_2},\ \mathrm{H_2 + C},\ \mathrm{CH + H},\ \mathrm{H + H + C}\} \tag{41}$$

associated to different *fragmentation channels* in which the geometry and the electronic states of the corresponding fragments is specified, as for example:

$$\mathrm{H_2 + C} = \left\{\ \mathrm{H_2(X\,^1\Sigma_g^+) + C(\,^3P)},\ \cdots,\ \mathrm{H_2}(a\,^2\Sigma_u^+) + \mathrm{C}(\,^1D),\ \cdots\ \right\}. \tag{42}$$

As higher energy ranges are studied, a larger number of isomers (energy order increasing) should be included. For the systems investigated in this paper and for internal energies covering a range from 0 eV up to 20 eV, two spin multiplicities per molecular geometry is enough (if they are stable). Then, for an easier description of the fragmentation using M_3C it is necessary to include all considered fragments grouped by chemical species.

3.2 Sampling State's Vector Space

Given an internal energy and a fragmentation model (a set of possible isomers including all the chemical species of interest) M_3C calculates the set of vector-states that are included into the region of maximum entropy; then the physical observables are obtained by performing a statistical average in this region. In each step of the Markov chain, the local DOS is calculated according to Eq. (36). Figure 2 shows the diagram of dependencies for the main values involved in the calculation of the local density of states $\Omega(E, \boldsymbol{\mathcal{X}})$. The quantities marked with the symbol $\circlearrowleft$ represent those variables that are sampled in a random way. When one of them is changed, all items connected by arrows are also updated/changed to compute $\Omega(E, \boldsymbol{\mathcal{X}})$,

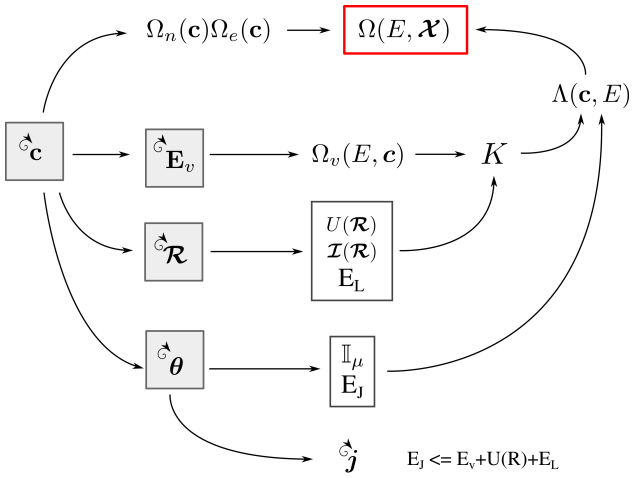

Figure 2: Schematic diagram showing the dependencies of the main quantities involved in the random sampling of the systems's state-vector $\boldsymbol{\mathcal{X}}$ according to the $\Omega(E, \boldsymbol{\mathcal{X}})$ distribution. See text for details.

For a specific molecular system, there are several changes that one can carry out to explore the state-vector space in the Markov chain. Our choice is based on a physical meaning and on the dependencies diagram shown in the Fig. 2. In order to design the Markov chain, we associate the different contributions to the DOS with abstract objects called reactors. One introduces a set of molecules (reactants) into one of these reactors and one gets a set of molecules (products) with new properties; for instance, changes in the vibrational excitation or in the chemical composition can be obtained.

The *vibrational reactor* ($\hat{V}$) is responsible for the random sampling of the vibrational energy for each fragment. The effect on the state $\boldsymbol{\mathcal{X}}$ can be represented as

$$\hat{V}\boldsymbol{\mathcal{X}} \rightarrow \boldsymbol{\mathcal{X}}' : (\mathbf{c}, \mathbf{E}'_v, \boldsymbol{\mathcal{R}}, \boldsymbol{\theta}) \, . \tag{43}$$

In the *rotational reactor* ($\hat{R}$) the orientation of the individual fragments are sampled in a random way from a uniform distribution, and the angular momentum couplings between molecules are computed by taking into account the conservation of the total angular momentum. This reactor also carries out a transformation of the inertia tensors according to the coordinate reference system:

$$\hat{R}\boldsymbol{\mathcal{X}} \rightarrow \boldsymbol{\mathcal{X}}' : (\mathbf{c}, \mathbf{E}_v, \boldsymbol{\mathcal{R}}, \boldsymbol{\theta}') \, . \tag{44}$$

The *translational reactor* ($\hat{T}$) samples the position of each fragment employing two possible algorithms: (i) a random-walker algorithm, where the position of the fragments is sampled allowing changes within a sphere of radius $\Delta\boldsymbol{\mathcal{R}}$, centered on its previous position $\boldsymbol{\mathcal{R}}$ ($\boldsymbol{\mathcal{R}} \rightarrow \boldsymbol{\mathcal{R}} + \Delta\boldsymbol{\mathcal{R}}$), (ii) a completely random algorithm, where any change in the position of the fragment is possible: $\boldsymbol{\mathcal{R}} \rightarrow \boldsymbol{\mathcal{R}}'$. In this reactor, the corresponding interaction energy between fragments (potential energy function) is computed with the new positions:

$$\hat{T}\boldsymbol{\mathcal{X}} \rightarrow \boldsymbol{\mathcal{X}}' : (\mathbf{c}, \mathbf{E}_v, \boldsymbol{\mathcal{R}}', \boldsymbol{\theta}) \, . \tag{45}$$

The *structure reactor* calculates the possible fragmentation patterns by satisfying the composition and charge conservation rules. The algorithm is based on a random search tree over all possible fragments provided by the user. The change in the number of fragments can be chosen within an input parameter n:

$$\hat{S}_n \boldsymbol{\mathcal{X}} \rightarrow \boldsymbol{\mathcal{X}}' : (\mathbf{c} + \Delta\mathbf{n}, \mathbf{E}'_v, \boldsymbol{\mathcal{R}}', \boldsymbol{\theta}') \; . \tag{46}$$

In this way, the Markov chain with N steps can be written as the product of an irreducible set of reactors ($\hat{S}_1\hat{T}\hat{R}\hat{V}$) as follows,

$$\begin{gathered} \boldsymbol{\mathcal{X}}_0 \overset{\hat{V}}{\rightarrow} \boldsymbol{\mathcal{X}}_1 \overset{\hat{R}}{\rightarrow} \boldsymbol{\mathcal{X}}_2 \overset{\hat{T}}{\rightarrow} \boldsymbol{\mathcal{X}}_3 \overset{\hat{S}_1}{\rightarrow} \boldsymbol{\mathcal{X}}_4 \overset{\hat{V}}{\rightarrow} \boldsymbol{\mathcal{X}}_5 \overset{\hat{R}}{\rightarrow} \cdots \\ MC : \left[\prod_{i=1}^{N/4} \hat{S}_1\hat{T}\hat{R}\hat{V} \right] \boldsymbol{\mathcal{X}}_0 \; . \end{gathered} \tag{47}$$

Typically the Markov chain must be modified so that the average acceptance ratio is roughly 30-50%. Too small values of this parameter result in a slow exploration of the phase space. Too large will result in configurations without statistical meaning.

4 Applications

In this section we illustrate the capabilities of the M_3C code. We start by considering a simple system, a neutral cluster of Ar atoms, for which the interatomic potential is known and there exist previous theoretical calculations to compare with .[64,75,76] To check the validity of our new implementation in such weakly bound systems, we have computed several thermodynamic properties. The second kind of systems we analyze is small neutral carbon clusters, for which there is accurate experimental information on fragmentation branching ratios.[44] In this case we apply a molecular description of the different fragments and dissociation channels that can be produced when these carbon clusters are highly excited. We then consider

fragmentation of small singly positively charged carbon clusters and of charged molecules containing different kinds of atoms. In both cases, comparison with available experimental fragmentation yields [77–80] will be carried out in order to validate our new methodology.

4.1 Caloric Curve for Ar_{13}

A recurrent topic in cluster physics is the identification and characterization of phase transitions, including solid-to-liquid and liquid-to-gas phase transitions. Since clusters are particles of finite size, the question of how to detect and/or characterize such transitions is a conceptual challenge. Schmidt and co-workers[81] reported the first experimental determination of a caloric curve for the melting transition in a small cluster. Specifically, they studied a singly-charged sodium cluster with 139 atoms. Other experimental and theoretical studies on the thermodynamic properties of metallic clusters have also been reported (see for example[39,82–84]) and their properties are nowadays well understood. However, in the case of small weakly bound clusters, experimental caloric curves are much harder to obtain and the theoretical simulations play a very important role to analyze such transitions. The first application of our method is to compute the caloric curve of the argon cluster Ar_{13}. For this system, theoretical studies have been published before by using Molecular Dynamics and Monte-Carlo simulations (see for example [64,75,76]).

We monitor the occurrence of a phase transition in the caloric curve $T(E)$ (temperature versus internal energy) and its heat capacity $C_v(T)$. The caloric curve $E(T)$ was obtained by computing the temperature at different internal energies. According to the thermodynamic definition of temperature (in the microcanonical ensemble), it can be easily calculated by using the following equation

$$T = \frac{\partial \mathcal{S}}{\partial E} = \left\langle \frac{s/2 - 1}{K} \right\rangle^{-1} \tag{48}$$

where K is the kinetic energy, s the number of degrees of freedom (see Eq. (37)) and $\langle\rangle$

represents the averaging over an entire simulation. The heat capacity $C_v(T)$ was calculated as the first derivative of $E(T)$ (previously smoothed with a "natural spline interpolation"):

$$C_v = \frac{\partial E}{\partial T} \tag{49}$$

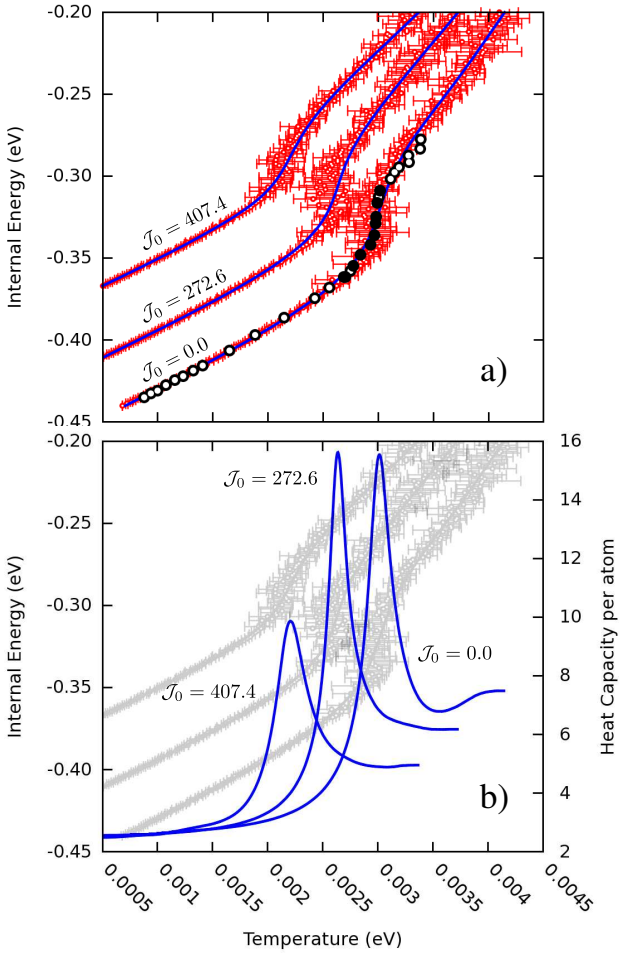

Figure 3: Computed microcanonical caloric curve for Ar_{13}. a) The excitation energy is plotted as a function of the temperature for three values of total angular momentum $\boldsymbol{\mathcal{J}}_0$. Red points and their errors bars (standard deviation) are the direct results of the simulations. Blue solid lines are a fit obtained with a "natural spline interpolation". Black circles correspond to the caloric curve calculated by Jellinek *et. al.*[35] In the coexistence region, filled circles are used. b) Heat capacity as a function of the temperature. Blue solid lines are the heat capacities obtained as first derivative of the caloric curves (gray). Notice that the melting temperatures T =0.00299, 0.00268 and 0.00221 eV (0.29, 0.26 and 0.21 in LJ units) appear for $|\boldsymbol{\mathcal{J}}_0|$ =0.0, 272.6, and 407.4 a.u. (0, 8, and 12 in LJ units) respectively.

In this case we only considered one possible fragment, the argon atom. The initial

positions of the atoms in the Ar_{13} cluster were taken from the geometry reported in "The Cambridge Cluster Database" (tightly-bound icosahedral cluster).[85,86] For the lowest internal energies, a random-walker-radius ($\Delta\boldsymbol{\mathcal{R}}$) of 0.1 Å was necessary to prevent the evaporation of the cluster. This radius was gradually increased up to 0.3 Å for the highest values of internal energy. We also included a maximum overlapping radius of 0.2 Å to allow the system to reach the classical turning point. The 12-6 Lennard-Jones potential

$$U^{(2)}_{\mu\nu}(|\boldsymbol{\mathcal{R}}_{\mu\nu}|) = 4\varepsilon\left[\left(\frac{\sigma}{|\boldsymbol{\mathcal{R}}_{\mu\nu}|}\right)^{12} - \left(\frac{\sigma}{|\boldsymbol{\mathcal{R}}_{\mu\nu}|}\right)^{6}\right] \tag{50}$$

with $\varepsilon = 0.0104$ eV and $\sigma = 3.4\,\mathring{A}$[87] was employed to describe the inter-atomic Ar-Ar interactions. Simulations with Markov chains of $1.5\cdot10^5$ steps, using 10% of them as burn-in period and six replicas (or numerical experiments), were carried out for each value of the internal energy. In this example, only the simplest Markov chain was used, $\hat{T}$, *i.e.* only the translational reactor was used. Three values of $|\boldsymbol{\mathcal{J}}_0|$ were studied 0.0, 272.6 and 407.4 a.u., which are equivalent to 0, 8 and 12 in Lennard-Jones units respectively. These values were chosen in order to compare with results from Ref.[65] Here $\boldsymbol{\mathcal{J}}_0$ plays the same role as L because $\mathbf{J}_\mu = 0$ for all fragments. The $|\boldsymbol{\mathcal{J}}_0|$ vector was always in the direction of the larger inertia moment of the system.

Fig. 3a shows the calculated caloric curves for the Ar_{13} system, including standard deviations. The results show that, at $T \sim 0.02 - 0.03$ eV, a large amount of energy is needed to increase the temperature. This range of temperatures comprises a region where two phases coexist: solid-like and liquid-like, which is consistent with previous theoretical studies (see for example [58,65,87]). The Figure also shows a comparison with the caloric curve obtained by Jellinek *et. al.*[35] for the case of $|\boldsymbol{\mathcal{J}}_0| = 0$. The agreement between both sets of results is evident. Our results in the coexistence region exhibit larger error bars, because both phases compete during the calculation of the average temperature and it is not possible to distinguish them. Fig. 3b shows the heat capacity per atom as a function of temperature, $C_v(T)$. At low temperature, $C_v(T)$ is approximately constant and close to the value predicted by

the harmonic approximation: the number of degrees of freedom per atom, $s/13 \sim 2.54$. In the range $T \sim 0.02 - 0.03$ eV, the system leaves the crystalline structure and acquires a disordered liquid-like behavior, where the melting temperature is indicated by the peak of the curve. For larger values of temperature, the system reaches its fluid phase entirely where $C_v(T)$ is again approximately constant. Our results agree fairly well with those previously reported in[65] for the same values of $\boldsymbol{\mathcal{J}}_0$. Melting temperatures T =0.00299, 0.00268 and 0.00221 eV (0.29, 0.26 and 0.21 in LJ units) are obtained for $|\boldsymbol{\mathcal{J}}_0|$ =0.0, 272.6, and 407.4 a.u. (0, 8, and 12 in LJ units), respectively. That is, the melting temperature decreases with the total angular momentum, and so does the peak-transition width. These results show that the new M_3C scheme can predict the thermodynamic properties of weakly bound systems with high accuracy.

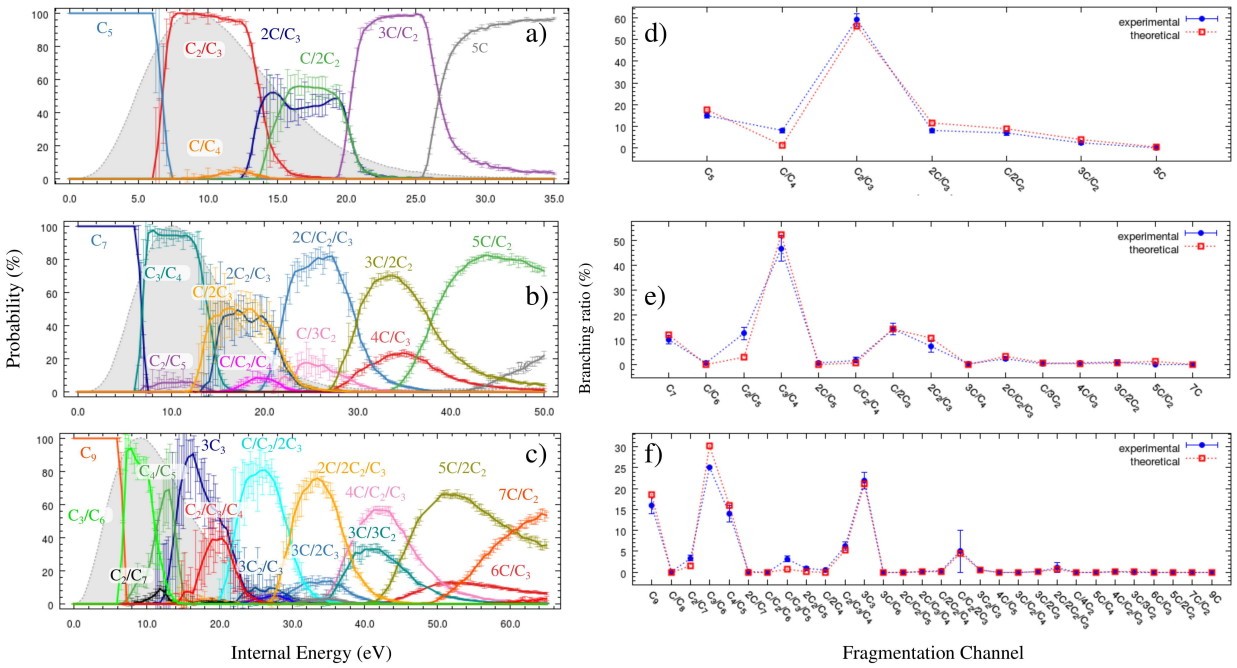

Figure 4: Fragmentation of C_n ($n = 5, 7, 9$) molecules from M3C simulations and comparison with experiment. Panels a), b) and c): Channel probabilities as a functions of the internal energy (breakdown curves) for C_5, C_7 and C_9, respectively. The points represent an average value over 6 different runs and their vertical error bars correspond to the standard deviation. Panels d), e) and f): Branching ratios for C_5, C_7 and C_9 respectively. Blue full circles and their error bars, experiment from.[44] Red open squares, theoretical results obtained by convolution with the fitted energy distribution functions shown in gray on left panels. Dashed lines are to guide the eye.

4.2 Fragmentation Spectrometry of Neutral Carbon Clusters C_n ($n = 5, 7, 9$)

Carbon-based molecules are important in many astrophysical environments such as the interstellar medium or planetary atmospheres, and they have been the subject of intense theoretical and experimental research (see, for example,[46,88–91] and references therein). From the experimental point of view, a very important research activity has been carried out by the group of Béroff and Chabot.[92–94] In these experiments, excited carbon clusters are formed by charge transfer reactions in collisions of charged carbon clusters with helium atoms and the subsequent fragmentation yields are measured. Here, we will compare the results of our simulations with these measurements. The process can be summarized as follows:

$$\begin{aligned} C_n^+(E_0, K) + He(\varepsilon) &\rightarrow C_n(E_0 + E) + He^+(\varepsilon + K - E) \\ \\ C_n(E_0 + E) &\rightarrow C_{n-1} + C \\ &\rightarrow C_{n-2} + C_2 \\ &\rightarrow C_{n-1} + C + C \\ &\rightarrow \cdots \end{aligned} \tag{51}$$

being E_0 the initial internal energy of the cluster, K its kinetic energy and E the excess of internal energy after the collision. Our main hypothesis is that the fragmentation process is independent of the collision, since the former is much slower that the latter. The quantity that relates both processes is the energy distribution function $f(E)$, which tells us how likely is to deposit a given amount of energy E in the molecular target as a result of the collision. For short, we will call this function the deposited-energy function. This function contains all the physics related to the particular collision process that leads to excitation of the molecular target. Due to the large amount of available energy in such collisions, one can safely assume that $E_0 \ll E$, so that E_0 can be ignored.

These neutral carbon clusters were studied in the past by using our previous implementation of the MMMC method.[45] Thus, these results represent a very important source of

information for checking the validity of our model and therefore we will focus on the improvements that have been reached with the new implementation presented in this work. The first step in our simulations is to get all geometries for the possible fragments and their isomers. First, we made a stochastic search with 40 trials by using the M_3C interface with the molecular electronic structure code GAMESS.[72,95] These calculations were done at the DFT-B3LYP/6-311G level of theory. Then, by using the M_3C interface with the GAUSSIAN package,[73] this first guess of the molecular structures were refined at the DFT-B3LYP/6-311+G(3df) level of theory; vibrational frequencies were also obtained at the same level. We performed calculations for the two lowest spin multiplicities of all proposed structures. Finally, the electronic energies were obtained by using the more elaborate coupled cluster method CCSD(T)/6-311+G(3df). In total, we described the fragmentation of these molecules including 21, 43 and 68 possible fragments for C_5, C_7 and C_9, respectively. All optimized geometries are shown in the Supplementary Information (SI). They are in agreement with previous results.[89,96–102] With these structures, fragmentation models for $C_5/C_7/C_9$ can follow 7/15/53 fragmentation reactions including 85/247/401 fragmentation channels. As an example, the fragmentation model we used for the C_5 cluster is:

$$
\begin{aligned}
\mathrm{C} &= \{\ \mathrm{C}(^1D),\ \mathbf{C}(\mathbf{^3P})\ \} \\
\mathrm{C_2} &= \{\ \mathbf{C_2}(\mathbf{^1\Sigma_g^+}), \mathrm{C_2}(^3\Pi_u)\ \} \\
\mathrm{C_3} &= \{\ \mathbf{C_3}(\mathbf{^1\Sigma_g}), \mathrm{C_3}(^3A_1'),\ \mathrm{C_3}(^3A'')\ \} \\
\mathrm{C_4} &= \{\ \mathrm{C_4}(^1\Sigma_g),\ \mathrm{C_4}(^1A_g),\ \mathbf{C_4}(\mathbf{^1A'}),\ \mathrm{C_4}(^3\Sigma_g),\ \mathrm{C_4}(^3B_{3u}),\ \mathrm{C_4}(^3A_1)\ \} \\
\mathrm{C_5} &= \{\ \mathbf{C_5}(\mathbf{^1\Sigma_g}),\ \mathrm{C_5}(1\,^1A_1),\ \mathrm{C_5}(^1A_1'),\ \mathrm{C_5}(2\,^1A_1),\ \mathrm{C_5}(^3\Pi_g), \\
&\qquad\qquad \mathrm{C_5}(^3A),\ \mathrm{C_5}(^3B_2),\ C_5(^3A'')\ \}
\end{aligned}
\tag{52}
$$

Regarding the statistical simulation, we used a system radius of 8/9/10 Å, six numerical experiments with 1/3/10 $\times 10^5$ events each one and the sequence $5\hat{V}\hat{T}\hat{R}\hat{S}_0 5\hat{V}\hat{T}\hat{R}\hat{S}_{1:\text{-}1}$ as Markov chain (10% of burn-in period). The initial molecule was selected as the ground state

of $C_5/C_7/C_9$, which corresponds to a linear singlet isomer (`C5.q0.m1-1/C7.q0.m1-1/C9.q0.m1-1` see SI). An example of the M_3C input file for C_5 is available in the SI.

In order to compare our results with experimental measurements, the deposited-energy distribution $f(E)$ associated to the collision should be known. However, existing experimental approaches cannot provide this information for this kind of systems. Also, its evaluation from rigorous theoretical modeling of the collisions is nearly impossible. Here we will adopt the same strategy as in Refs.[44–46] and estimate the deposited-energy function from the comparison between the experimental fragmentation probabilities (intensities in mass spectrum) and the computed M_3C probabilities. The mathematical description of the fitting procedure used to obtain this function is explained in detail in the SI. We do not introduce any constraint about how this function should be, except that 1) the function should only exhibit a single maximum, 2) it should decrease monotonically as the excitation energy increases, and 3) it should go to zero at the origin. These are typical characteristics of the few deposited-energy distribution that have so far been determined experimentally.[47,49] We notice that the $f(E)$ function is very similar for the three systems investigated in this subsection (see Fig. 4a-c), which is compatible with the fact that the measurements were performed under the same experimental conditions. They are also very similar to those used in Ref.,[44] which were based on semi-empirical arguments. We also notice that, if the calculated M_3C probabilities were wrong, a fit to a function fulfilling the above three restrictions would be impossible.

In general, C_5, C_7, and C_9 clusters do not dissociate up to ∼6 eV. In the range of excitation energy ∼6-15 eV, the dominant dissociation channels are C_3/C_2, C_3/C_4, and C_3/C_6 respectively, but C_4/C_5 is also significantly observed for C_9. The probability for the loss of a carbon atom is, in all cases, practically zero in this energy range. At higher energies, (∼15-20 eV for C_5, ∼20-30 eV for C_7 and ∼30-40 eV for C_9) fragmentation channels leading to C_3 have a higher probability. Notice also that in this energy range, channels leading to C_2 become dominant when the excitation energy increases. These trends can be understood in terms of the energy sharing among the fragments (see SI). Fragmentation channels involving

C_3 are more important in energy regions where the vibrational contribution is larger than the rotational one. However, in channels involving C_2 the rotational component of the energy is larger than the vibrational one. The swapping takes place at ∼20 eV, ∼30 eV, and ∼35 eV for C_5, C_7, and C_9 respectively.

An earlier implementation of the MMMC method[45] allowed us to understand the main factors governing the fragmentation of small carbon clusters and to extract the energy deposited in the collision.[44–46,103] The main improvements considered in the present implementation are: 1) the angular momentum constraint $\boldsymbol{\mathcal{J}} = \mathbf{0}$ is now fully satisfied, and 2) many more isomers have been considered. We discuss both contributions separately.

Regarding the angular momentum scheme used to fulfill the condition $\boldsymbol{\mathcal{J}} = \mathbf{0}$, in this work we have used $\mathbf{L} + \sum_{\mu=1}^{N_f} \mathbf{J}_\mu = \mathbf{0}$, instead of $\sum_{\mu=1}^{N_f} \mathbf{J}_\mu = \mathbf{0}$ as in previous work. If we rewrite these constraints as follows: $\mathbf{L} = -\sum_{\mu=1}^{N_f} \mathbf{J}_\mu$ and $\mathbf{J}_{N_f} = -\sum_{\mu=1}^{N_f-1} \mathbf{J}_\mu$, respectively, it is apparent that, in the first case, all the angular-momenta vectors are independent, while, in the second case, only the $N_f - 1$ momenta are independent. This means that, if the angular momenta values are changed, the vectors J_{N_f} and $\mathbf{L}$ should be changed as well in order to satisfy the angular momentum conservation constraint (since these ones are used to compensate the first ones). Thus, in the previous implementation, the contribution of the angular momenta to the DOS from the N_f-th fragment was ignored and now we include it. The most important effect of this improvement can be clearly appreciated on the tails observed in the breakdown curves at high excitation energy, which now are longer and more pronounced. For instance, in the fragmentation of the C_5 cluster, channels $3C/C_2$ and 5C are in competition in the transition region at ∼ 26 eV (see Fig. 4a). In the new implementation, the probability to find the $3C/C_2$ channel extends by ∼ 5 eV at higher energies before it goes to zero, while in Ref.,[45] this probability is reduced suddenly. Basically, when $\mathbf{L}$ is used to compensate the angular momenta, the C_2 fragment may exchange energy with other rotational and translational components, allowing for a gradual fragmentation. A similar effect is observed in the high energy region of the fragmentation curves for C_7 and C_9. In

all cases, the first breaking of the parent molecule is less abrupt than reported earlier[45] (see Fig. 4a-c). This improvement also reflects in the appearance of new fragmentation channels, which were not visible in Ref.[45] In particular, the C/C_4 channel resulting from the fragmentation of C_5 (Fig. 4a) is now quite apparent, which agrees better with the experimental observations. The rotational contribution of C_4 allows for an increase of the global probability for this channel, which increases from zero to $\sim$5% with respect to the previous calculations. However, this is not enough to account for the contribution of $\sim 20\%$ observed in the experiment (Fig. 4d). Channels $2C/C_2/C_3$ for C_7 and C_4/C_5 for C_9, also present increased probabilities; and channels $C/C_2/C_4$ for C_7, and C_2/C_7,$C_2/C_3/C_4$ for C_9 show a non-zero contribution. In all cases, the new results improve on the existing calculations and lead to a better agreement with experiments (see Fig.4e-f).

Regarding the number of isomers, in our earlier work we only considered two spin multiplicities (singlet and triplet states) and two structural isomers (linear and cyclic geometries) for each fragment, while we are now including many more isomers, 21/43/68 in contrast with 16/24/32 for $C_5/C_6/C_7$, respectively. The present results indicate that the new considered isomers participate in less than $\sim$10% of the fragmentation probabilities. Thus, $\sim$90% of results obtained by only considering one linear and one cyclic isomer for a given value of spin and multiplicity correctly reproduce the experiment. As a general trend, the breakdown curves are not drastically affected. We have found, however, an exception: for the C_4 fragment, the singlet isomer with a planar structure in which three carbon atoms are attached to the same central carbon atom (see `C4.q0.m1-3` at SI) plays a very important role in the fragmentation of $C_n(n = 5, 7, 9)$. This isomer has been well described theoretically[102] and also detected in Coulomb explosion experiments.[104] In almost all cases this isomer contributes about 50% to the signal in channels where the fragment C_4 participates, specifically C/C_4 for C_5, $C/C_2/C_4$ for C_7 and $C_2/C_3/C_4$ for C_9. In the special case of channel C_4/C_5 for C_9, this isomer does not play any role; the largest contribution in this channel comes from the linear triplet isomer (see `C4.q0.m3-1` at SI). Thus, the larger probability observed in this

channel is exclusively due to the new angular momentum scheme included in the current implementation.

In summary, these results show that a correct implementation of the angular momentum conservation improves significantly the description of the fragmentation of neutral carbon clusters.

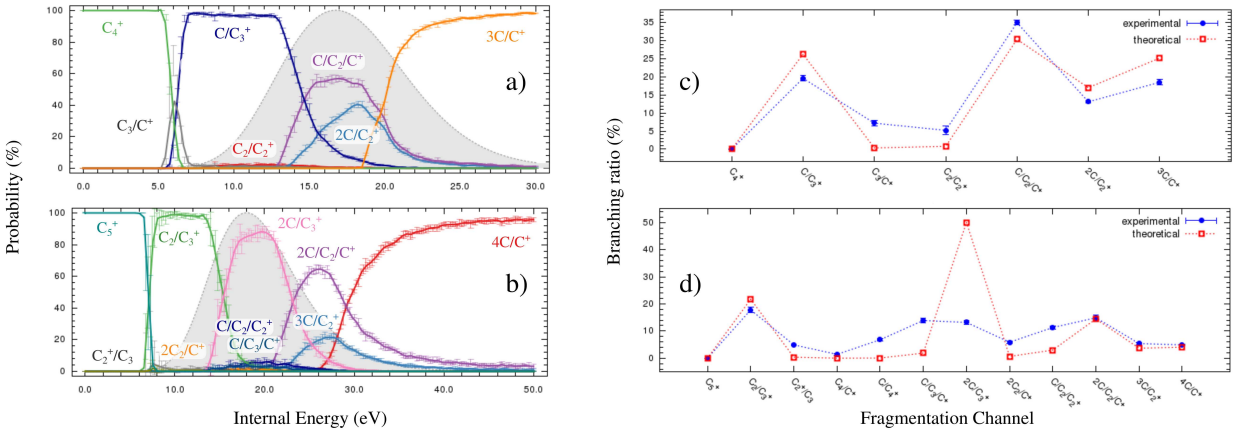

Figure 5: Fragmentation of C_n^+ $(n = 4, 5)$ molecules from M3C simulations and comparison with experiment. Panels a), b): Channel probabilities as a functions of the internal energy for C_4^+ and C_5^+, respectively. The points represent an average value over 6 different runs and their vertical error bars correspond to the standard deviation. Panels d), e): Branching ratios for C_4^+ and C_5^+, respectively. Blue full circles and their error bars, experimental results for.[79] Red open squares and green points, theoretical results obtained by convolution with the fitted energy distribution functions shown in gray on left and center panels, respectively. Green points, represent the results obtained when potential energy curves are considered, red open squares otherwise. Dashed lines are to guide the eye.

4.3 Fragmentation Spectrometry of Singly Charged Carbon Clusters C_n^+ $(n = 4, 5)$

Experimental works focussed in fragmentation of charged carbon clusters have been also carried out by the group of Béroff and Chabot[79,105] by measure the branching ratios of all possible fragmentation channels. In this case, excited singly charged carbon clusters are experimentally obtained in collisions with helium atoms following a dissociative excitation

process, according to the following scheme:

$$\mathrm{C}_n^+(E_0, K) + \mathrm{He}(\varepsilon) \rightarrow \mathrm{C}_n^+(E_0 + E) + \mathrm{He}(\varepsilon + K - E)$$

$$\begin{aligned} \mathrm{C}_n^+(E_0 + E) &\rightarrow \mathrm{C}_{n-1}^+ + \mathrm{C} \\ &\rightarrow \mathrm{C}_{n-1} + \mathrm{C}^+ \\ &\rightarrow \mathrm{C}_{n-2} + \mathrm{C}^+ + \mathrm{C} \\ &\rightarrow \cdots \end{aligned} \tag{53}$$

Note that, unlike for neutral carbon clusters, new channels appear in the fragmentation of singly charged carbon clusters, such as $\mathrm{C}_{n-1}^+/\mathrm{C}$ and $\mathrm{C}_{n-1}/\mathrm{C}^+$. This means that, in addition to the combinatorial problem associated with the number of bonds that can be broken, it is necessary to include an extra degree of freedom to describe how the charge is distributed among the different fragments. Many of the channels leading to different charge distributions are close in energy but the measured branching ratios are substantially different. For example, channels $\mathrm{C}_3/\mathrm{C}^+$ and $\mathrm{C}_3^+/\mathrm{C}$, in the fragmentation of C_4^+, are only 0.3 eV apart from each other, but their branching ratios are 7.2% and 19.6%, respectively.[79] Hence, analysis solely based on energetic criteria are not adequate to explain this behavior. Fragmentation of singly-charged carbon clusters is thus a more stringent test of the M3C approach.

We have studied the fragmentation of these systems employing the same computational setup as for neutral carbon clusters. In the stochastic search, we found 2, 2, 4, 5 and 7 isomers for C^+, C_2^+, C_3^+, C_4^+ and C_5^+ respectively, all of them are shown in the SI. The fragmentation model also includes the corresponding isomers of the neutral carbon clusters.

For example, the fragmentation model employed to study C_4^+ is:

$$
\begin{aligned}
\mathrm{C} &= \{\ \mathrm{C}(^1D),\ \mathbf{C}(\mathbf{^3P})\ \} \\
\mathrm{C}^+ &= \{\ \mathrm{C}^+(\mathbf{^2P}),\ \mathrm{C}^+(^4P)\ \} \\
\mathrm{C}_2 &= \{\ \mathbf{C_2}(\mathbf{^1\Sigma_g^+}),\ \mathrm{C}_2(^3\Pi_u)\ \} \\
\mathrm{C}_2^+ &= \{\ \mathbf{C_2^+}(\mathbf{^4\Sigma_g^-}),\ \mathrm{C}_2^+(^2\Pi_u)\ \} \\
\mathrm{C}_3 &= \{\ \mathbf{C_3}(\mathbf{^1\Sigma_g}),\ \mathrm{C}_3(^3A_1'),\ \mathrm{C}_3(^3A'')\ \} \\
\mathrm{C}_3^+ &= \{\ \mathbf{C_3^+}(\mathbf{^2B_2}),\ \mathrm{C}_3^+(^2\Sigma),\ \mathrm{C}_3^+(^4A_1'),\ \mathrm{C}_3^+(^4\Pi_u)\ \} \\
\mathrm{C}_4^+ &= \{\ \mathbf{C}_4^+(^1\Sigma_g),\ \mathrm{C}_4^+(^1A_1),\ \mathrm{C}_4^+(^1A'),\ \mathrm{C}_4^+(^3\Sigma_g),\ \mathrm{C}_4^+(^3B_{3u}),\ \mathrm{C}_4^+(^3A_1), \\
&\qquad \mathrm{C}_4^+(^2\Pi_g),\ \mathbf{C_4^+}(\mathbf{^2A'}),\ \mathrm{C}_4^+(^4B_{3u}),\ \mathrm{C}_4^+(^4A_2),\ \mathrm{C}_4^+(^4B_1)\ \}
\end{aligned}
\tag{54}
$$

In total we used 20 and 33 molecules to describe the fragmentation of C_4^+ and C_5^+ respectively. With this fragmentation model, C_4^+ and C_5^+ may follow 15 and 53 fragmentation reactions or 247 and 401 fragmentation channels correspondingly. The initial state was selected as the corresponding ground state. C_4^+ has a cyclic doublet isomer (`C4.q1.m2-2` see SI) and C_5^+ a linear doublet (`C5.q1.m2-1` see SI). We also compare with previous experimental results.[79]

In this kind of systems, the most complicated part is to describe the charge distribution into fragments with the same stoichiometry, *e.g.* $C_{n-m}^+ + C_m$ versus $C_{n-m} + C_m^+$. Experimental branching ratios indicate that, in general, the most probable configuration corresponds to the case where the charge goes onto the heaviest fragment (see Fig.5). On the other hand, the computed lowest dissociation energies indicate that the energetically most favorable channels are C^+/C_3 (4.8 eV) and C_2/C_3^+ (6.5 eV), for C_4^+ and C_5^+ respectively. Thus, dissociation energies only correlate with experimental branching ratios for the C_5^+ case.

To simulate the fragmentation of these molecules, we have used the hard-sphere model (HSM, default option in M_3C) to represent the inter-fragment interactions, by using the same strategy as for neutral carbon clusters. Panels a-b on Fig. 5 show the breakdown

curves obtained for the fragmentation of these systems. If we first concentrate on those channels leading to two fragments, we can see that the C^+/C_{n-1} channel opens before the C/C^+_{n-1} one for $n = 4$ ($\sim$7 eV) and that the C_2/C_3^+ channel opens practically at the same energy as the C_2^+/C_3 one ($\Delta E = 0.1$ eV) for C_5^+. However, for both systems, those channels where the charge is located on the heaviest fragment rapidly increase their probability in the range 7-15 eV (C/C_3^+ and C_2/C_3^+, respectively). Actually, by analyzing contributions to the DOS (see SI), we observe that this behavior is a consequence of a larger contribution from the vibrational part of C_3^+, since their harmonic frequencies are significantly smaller than those of C_3 (155 cm^{-1} and 20 cm^{-1} respectively). In contrast, for C_2, the rotational contribution is dominant, since its smaller bong length leads to an increase in the DOS (due to the increase in the inertia tensor elements). The three-fragments region of C_5^+ is again dominated by the high contribution to the DOS by vibrations, due to the presence of the C_3^+ fragment in the most probable channel. The four/three-fragments region for C_5^+/C_4^+ is mainly governed by the Gibbs' correction factor, which reduces significantly the probability of those channels containing indistinguishable fragments. Thus, the probability of $3C/C_2^+$ is smaller than that of $2C/C_2/C^+$ for C_5^+, and the probability of $2C/C_2^+$ is smaller than that of $C/C_2/C^+$ for C_4^+.

Comparison of these results with the experimental branching ratios is carried out after convolution of the probabilities with the deposited-energy function (also shown in Fig. 5). This function has been derived by using the same procedure as in the preceding subsection. We see a very good agreement for C_4^+. However, for C_5^+, the simulations overestimate the $2C/C_3^+$ channel. The possible origin of this discrepancy can be found with the help of Fig. 6. The red lines represent the default interacting potential used by M_3C and the black lines the real potential energy curves that describe the charge distribution into the dissociative channels. As can be seen, for C_5^+, the simple M_3C potential cannot account for the crossing between the states that ultimately dictates the relative probability of fragmentation channels that place the charge in one center or the other. To avoid this problem, one might then use

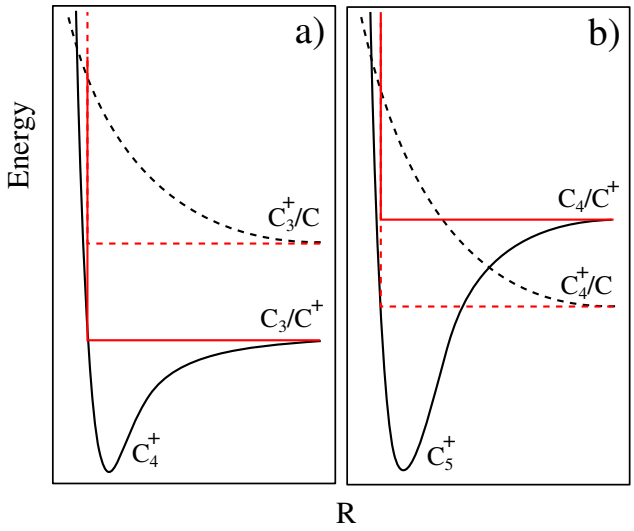

Figure 6: Schematic view of potential-energy curves for loss of atomic carbon in linear a) C_4^+ and b) C_5^+.

the actual potential energy surfaces of the system. However, computing these surfaces for the C_n^+ molecules is not a simple task due to symmetry-breaking problems (see[106] and references therein). In the C_n^+ linear clusters, electronic states described at the B3LYP level suffer from spatial symmetry breaking since for this electronic state the unpaired electron is essentially localized on the terminal carbon atoms. Thus, these structures can only be described by two resonant structures, which means that one has to deal in fact with a multi-reference problem and use expensive methods such as CASSCF, CASPT2, MRCI, etc. Computing the potential energy surfaces for all the fragmentation channels including all the isomers is computationally prohibitive.

All in all, the present results, which are the first ones ever computed for fragmentation of charged carbon clusters, catch all the essential features and, for the smaller system $C4^+$, lead to an excellent quantitative agreement with the experimental results.

4.4 Mass Spectrometry of C_2H_2

The last example of the M_3C capabilities is the simulation of molecular mass spectra. For this we have chosen the acetylene molecule, C_2H_2, whose mass spectrum is available from the

NIST Mass Spectrometry Data Center.[80] In the experimental setup, accelerated electrons (typically with $\sim 70 - 100$ eV of energy) collide with the neutral molecules in gas phase producing excitation+ionization. The excited and ionized molecule undergoes fragmentation and the intensity of the cationic fragments produced are recorded as a function of their mass over charge ratio (m/z). The process can be summarized as follows:

$$\begin{aligned} \mathrm{C_2H_2}(E_0) + e^-(\varepsilon) &\rightarrow \mathrm{C_2H_2^+}(E_0 + E) + 2e^- \\ \\ \mathrm{C_2H_2^+}(E_0 + E) &\rightarrow \mathrm{C_2H^+ + H} \\ &\rightarrow \mathrm{C_2^+ + H_2} \\ &\rightarrow \mathrm{C}H^+ + \mathrm{CH} \\ &\rightarrow \cdots \end{aligned} \tag{55}$$

To obtain the corresponding mass spectrum, one must simulate the fragmentation process of the $\mathrm{C_2H_2^+}$ cation, convoluted as usual with the energy distribution function $f(E)$ (see SI for details). The first step in our simulations is to get all geometries for the possible fragments and their isomers. First, we made a stochastic search by using the $\mathrm{M_3C}$ interface with the molecular electronic structure code GAMESS.[71,72] These calculations were done at the DFT-B3LYP/6-311G level of theory. We increased gradually the number of trials from 20 until convergence in the number of different isomers was achieved. Then, by using the $\mathrm{M_3C}$ interface with the GAUSSIAN package,[73] this first guess of molecular structures were refined at the DFT-B3LYP/6-311+G(3df) level of theory; vibrational frequencies were also obtained at this level of theory. Finally, the electronic energies were obtained by using the coupled cluster theory CCSD(T)/6-311+G(3df), which includes all single and double excitations, as well as triple excitations in a perturbative way. Once all structures, electronic energies (including wave function symmetry) and vibrational frequencies for all possible fragments were computed, we used them to build the $\mathrm{M_3C}$ input file (see SI for details). In total, we described the fragmentation of this molecule including 31 molecules (geometries for each

considered molecule can be found in the SI); energy and geometry for these molecules are in agreement with previously reported data in the literature.[107–111] We only considered the two lowest spin multiplicities. The fragmentation model we used is:

$$
\begin{aligned}
\mathrm{H} &= \{\ \mathbf{H}(\,^{\mathbf{2}}\mathrm{S})\ \} \\
\mathrm{C} &= \{\ \mathrm{C}(\,^{1}D),\ \mathbf{C}(\,^{\mathbf{3}}\mathbf{P})\ \} \\
\mathrm{H_2} &= \{\ \mathbf{H_2}(\,^{\mathbf{1}}\mathbf{\Sigma_g^+})\ \} \\
\mathrm{CH} &= \{\ \mathbf{CH}(\,^{\mathbf{2}}\mathbf{\Pi}),\ \mathrm{CH}(\,^{4}\Sigma_g)\ \} \\
\mathrm{C_2} &= \{\ \mathbf{C_2}(\,^{\mathbf{1}}\mathbf{\Sigma_g^+}),\mathrm{C_2}(\,^{3}\Pi_u)\ \} \\
\mathrm{CH_2} &= \{\ \mathrm{CH_2}(\,^{1}A_1),\ \mathbf{CH_2}(\,^{\mathbf{3}}\mathbf{B_1})\ \} \\
\mathrm{C_2H} &= \{\ \mathbf{C_2H}(\,^{\mathbf{2}}\mathbf{\Sigma_g}),\ \mathrm{C_2H}(\,^{2}A_1),\ \mathrm{C_2H}(\,^{4}A'')\ \} \\
\mathrm{H^+} &= \{\ \mathbf{H^+}\ \} \\
\mathrm{C^+} &= \{\ \mathbf{C^+}(\,^{\mathbf{2}}\mathbf{P}),\ \mathrm{C^+}(\,^{4}P)\ \} \\
\mathrm{H_2^+} &= \{\ \mathbf{H_2^+}(\,^{\mathbf{2}}\mathbf{\Sigma_g})\ \} \\
\mathrm{CH^+} &= \{\ \mathbf{CH^+}(\,^{\mathbf{1}}\mathbf{\Sigma}),\mathrm{CH^+}(\,^{3}\Pi)\ \} \\
\mathrm{C_2^+} &= \{\ \mathbf{C_2^+}(\,^{\mathbf{2}}\mathbf{\Pi_u}),\ \mathrm{C_2^+}(\,^{4}\Sigma_g^-)\ \} \\
\mathrm{CH_2^+} &= \{\ \mathbf{CH_2^+}(\,^{\mathbf{2}}\mathbf{A_1}),\ \mathrm{CH_2^+}(\,^{4}A_2),\ \mathrm{CH_2^+}(\,^{1}\Sigma_g)\ \} \\
\mathrm{C_2H^+} &= \{\ \mathrm{C_2H^+}(\,^{1}A'),\ \mathbf{C_2H^+}(\,^{\mathbf{3}}\mathbf{\Pi})\ \} \\
\mathrm{C_2H_2^+} &= \{\ \mathbf{C_2H_2^+}(\,^{\mathbf{2}}\mathbf{\Pi_u}),\ \mathrm{C_2H_2^+}(\,^{2}A'),\ \mathrm{C_2H_2^+}(\,^{4}B_g),\ \mathrm{C_2H_2^+}(2\,^{4}A_2),\ \mathrm{C_2H_2^+}(1\,^{4}A_2)\ \}
\end{aligned}
\tag{56}
$$

where isomers in bold indicate the corresponding ground state. With this fragmentation model, the excited $C_2H_2^+$ molecule may follow 17 fragmentation reactions in 117 different fragmentation channels, which are in competition all along the simulation. In the second step, we performed the statistical calculation itself. To this, we used a system radius of 8 Å, six numerical experiments with 6×10^4 events each and the sequence $5\hat{V}\hat{T}\hat{R}\hat{S}_0 5\hat{V}\hat{T}\hat{R}\hat{S}_{1:\text{-}1}$ as

Markov chain, using 10% of them as burn-in period. The ground state of $C_2H_2^+$ ($^2\Pi$) was selected as initial condition, which corresponds to a linear doublet isomer (`C2H2.q1.m2-2` see SI). The deposited energy function $f(E)$ was obtained by fitting to the experimental mass spectrum observed with electrons of 70 eV of kinetic energy[80] (see SI for details).

In panel a) of Fig. 7, we show the probability of the different fragmentation channels as a function of the internal energy. The intact molecule $C_2H_2^+$ does not dissociate up to ~ 6 eV. In the range of internal energy 6-8 eV, the CH_2^+/H channel is dominant, but in the range 8-12 eV it changes to C_2^+/H_2. Only these channels play a significant role, because, for larger energies, the $f(E)$ function is practically zero. Panel b) on the same figure shows the probability of appearance of the different charged fragments. In the range of excitation energy $6-12$ eV, we observe competition between C_2H^+ and C_2^+, being dominant the first one, with a small contribution of C_2H^+. This is in agreement with the experimental mass spectrum, where these three charged species are associated to the highest intensity peaks (see lower panel of Fig. 7).

The deposited-energy function $f(E)$ (top panel in Fig. 7) presents a maximum at ~ 4 eV. A comparison between the experimental mass spectrum (electron ionization) taken from NIST Mass Spectrometry Data Center[80] and our theoretical results convoluted with the above described energy distribution is shown in the lower panel of Fig. 7. In general, we observe a good agreement between theory and experiment, except for isotope peaks like M+1 at 27 m/z, which are not taken into account in our calculations.

An interesting option that this methodology offers is to perform an isomer analysis. For example, Fig. 7b shows the probability for all considered isomers of $C_2H_2^+$ as a function of the excitation energy. As can be seen, about 46% of the $C_2H_2^+$ peak in the mass spectrum corresponds to the vinylidene-like isomer ($^2A'$, `C2H2.q1.m2-1` see SI), $\sim$53% to the acetylene linear configuration ($^2\Pi$, `C2H2.q1.m2-2` see SI) and less than 1% to the three remaining isomers. It means that the most probable fragmentation pattern implies the existence of a transient isomerization mechanism of the molecular ion (acetylene$\rightarrow$vinylidene$\rightarrow$fragmentation).

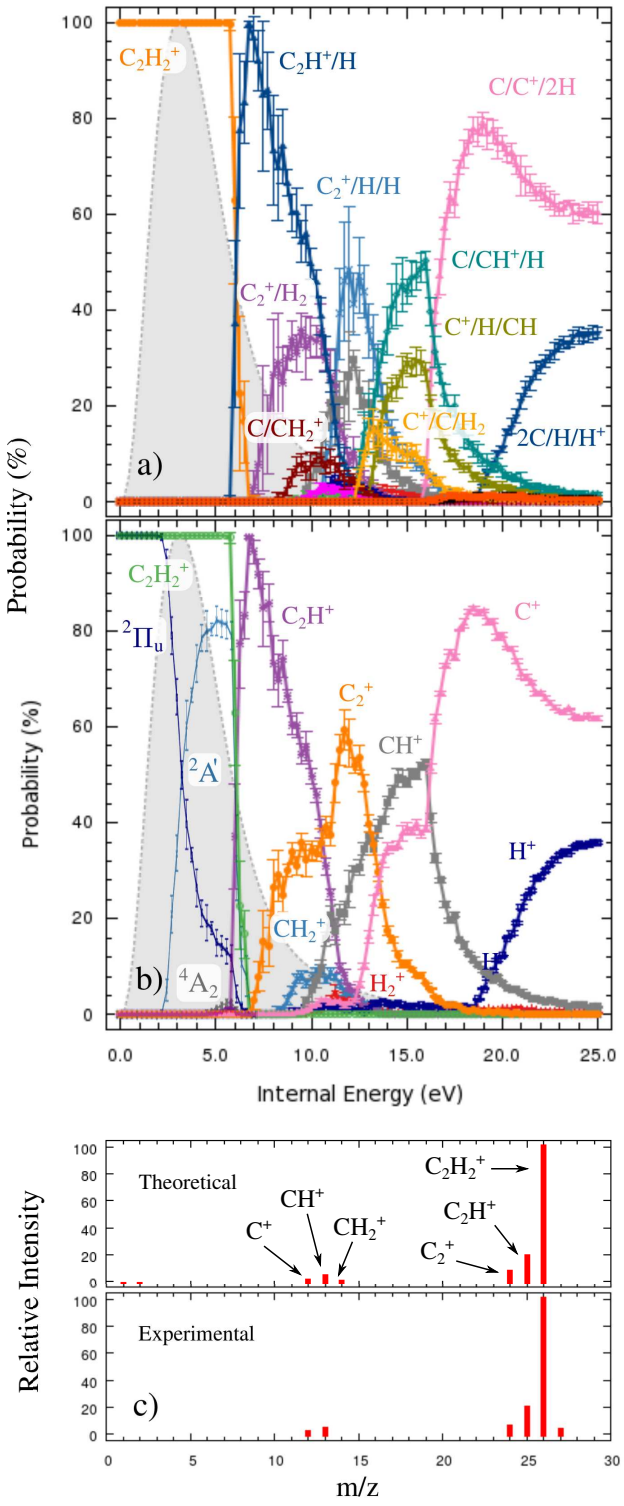

Figure 7: Fragmentation of the $C_2H_2^+$ molecule. a) Channels probabilities and b) species probabilities (only charged species are shown) as a function of the internal energy of the system. Isomer distribution for $C_2H_2^+$ is included ($^2\Pi_u$, $^2A'$ and $^4A_2$). c) Comparison between theoretical and experimental[80] mass spectrum. Last one was obtained by convolution with the deposited energy function which shown in gray on the upper panels.

Previous theoretical and experimental studies have reached a similar conclusion (see for example[112,113]).

5 Conclusion

We have presented a computational implementation of the Micro-canonical Metropolis Monte Carlo method, called M_3C, which can be applied to study fragmentation processes in a large variety of molecular and cluster systems irrespective of their composition and the nature of the chemical bonding between their elementary constituents. Its performance has been demonstrated by applying it to evaluate the caloric curve of the weakly bound rare gas cluster Ar_{13}, to simulate the mass spectra resulting from the bombardment of the acetylene molecule with fast electrons, and to interpret the yields observed in the fragmentation of both neutral and singly-charged carbon clusters in fast collisions with atomic species. Our results for singly-charged carbon clusters are the first ones to explain recent experimental observations for this kind of systems. Due to the generality of the M_3C implementation, application to more complicated systems is also possible. Calculations to understand fragmentation of protonated carbon clusters, sulfur clusters, and other large systems, for which existing experimental results remain unexplained, are already in progress.

In spite of these significant advances, there are a few more challenges that one should face in the near future. One of them is the application of the current M_3C methodology to study fragmentation of multiply charged molecules and clusters, where Coulomb explosion processes, which tend to split the charge among all possible fragments, compete with fragmentation channels where the charge exclusively remains in one of the fragments. An appropriate description of these processes requires accounting for Coulomb barriers, which is straightforward by using the M_3C methodology, but requires performing elaborate quantum chemistry calculations of transition states to determine the magnitude of such barriers. In this respect, the search of less time-consuming procedures to estimate the height and the

width of such barriers is highly desirable. Another challenge is to explore simple ways to incorporate non adiabatic effects that are involved in the crossings between potential energy surfaces leading to different dissociation limits, i.e., associated with fragmentation channels. As discussed in this paper for the case of singly charged carbon clusters, these crossings can strongly influence the fate of the charge in the fragmentation process, dictating if it goes to one or another fragment. Therefore, accounting for these non adiabatic effects can be crucial for an accurate evaluation of fragmentation yields in charged species. Work along these directions is already in progress in our laboratory.

Acknowledgement

We would like to thank Karine Béroff and Marin Chabot for enlightening discussions about fragmentation of carbon clusters and for useful comments on their experimental data. We acknowledge the generous allocation of computer time at the "Centro de Computación Científica at the Universidad Autónoma de Madrid" (CCC-UAM). Work supported by the MINECO projects FIS2013-42002-R and CTQ2013-43698-P, the CAM project NANOFRONTMAG-CM ref. S2013/MIT-2850S, and the European COST Action CM1204 XLIC. S.D.-T. gratefully acknowledges the "Ramón y Cajal" program of the Spanish MINECO. Financial support from the Spanish Ministry of Economy and Competitiveness, through The "María de Maeztu" Programme for Units of Excellence in R&D (MDM-2014-0377) is acknowledged.

Supporting Information Available

The following files are available free of charge.

- paperM3C-supplementary.pdf: Optimized geometry, symmetry and electronic state for each considered molecule, energy components analysis for $C_n (n = 5, 7, 9)$, DOS components analysis for $C_n^+ (n = 4, 5)$, M_3C input file for C_5, and the mathematical

description of the fitting procedure used to obtain the deposited energy functions.

This material is available free of charge via the Internet at `http://pubs.acs.org/`.

References

(1) Bardsley, J. N.; Mandl, F. *Rep. Prog. Phys.* **1968**, *31*, 471.

(2) Lutz, H.; Briggs, J. S.; Kleinpoppen, B. *Fundamental Processes in Energetic Atomic Collisions*; Nato Science Series B: Physics Vol 103; Springer US, 2012.

(3) Belkić, D. *Fast Ion-atom and Ion-molecule Collisions*; World Scientific. Singapore, 2013.

(4) Burke, P.; Joachain, C. *Photon and Electron Collisions with Atoms and Molecules*; Physics of Atoms and Molecules; Springer Science + Business Media, New York, 2012.

(5) Marr, G. *Handbook on Synchrotron Radiation: Vacuum Ultraviolet and Soft X-ray Processes*; Handbook on Synchrotron Radiation; Elsevier Science, Amsterdam, 2013.

(6) Kohl, J. *Experimental Studies in Molecular Fragmentation: Processes, Energetics and Diagnostics*; Defense Technical Information Center, Cambridge MA, 1983.

(7) Kirby, K. P. *Theoretical Studies in Molecular Fragmentation: Processes, Energetics and Diagnostics*; Defense Technical Information Center, Cambridge MA, 1987.

(8) Maurer, R. J. *Ionization and Fragmentation of Molecular Gases in Collisions with MeV/amu Heavy Ions*; Texas A & M University, 1988.

(9) Kushawaha, R.; Bapat, B. *Fragmentation Dynamics of Molecular Ions*; Lap Lambert Academic Publishing GmbH KG US, 2011.

(10) Whelan, C. *Fragmentation Processes: Topics in Atomic and Molecular Physics*; Cambridge University Press, New York US, 2013.

(11) Ullrich, J.; Shevelko, V. P. *Many-Particle Quantum Dynamics in Atomic and Molecular Fragmentation*; Springer Series on Atomic, Optical, and Plasma Physics; Springer-Verlag Berlin Heidelberg, 2013.

(12) Chen, T. *Ions Colliding with Molecules and Molecular Clusters: Fragmentation and Growth Processes*; Fysikum, Ph.D. Thesis, Stockholm university, Sweden, 2015.

(13) Schinke, R. *Photodissociation Dynamics: Spectroscopy and Fragmentation of Small Polyatomic Molecules*; Cambridge Monographs on Atomic, Molecular and Chemical Physics; Cambridge University Press, New York US, 1995.

(14) Kling, M. F.; Vrakking, M. J. *Annu. Rev. Phys. Chem.* **2008**, *59*, 463–492.

(15) Calegari, F.; Ayuso, D.; Trabattoni, A.; Belshaw, L.; De Camillis, S.; Anumula, S.; Frassetto, F.; Poletto, L.; Palacios, A.; Decleva, P.; Greenwood, J. B.; Martín, F.; Nisoli, M. *Science* **2014**, *346*, 336.

(16) Jiang, Y. H.; Rudenko, A.; Herrwerth, O.; Foucar, L.; Kurka, M.; Kühnel, K. U.; Lezius, M.; Kling, M. F.; van Tilborg, J.; Belkacem, A.; Ueda, K.; Düsterer, S.; Treusch, R.; Schröter, C. D.; Moshammer, R.; Ullrich, J. *Phys. Rev. Lett.* **2010**, *105*, 263002.

(17) Zettergren, H.; Rousseau, P.; Wang, Y.; Seitz, F.; Chen, T.; Gatchell, M.; Alexander, J. D.; Stockett, M. H.; Rangama, J.; Chesnel, J. Y.; Capron, M.; Poully, J. C.; Domaracka, A.; Méry, A.; Maclot, S.; Schmidt, H. T.; Adoui, L.; Alcamí, M.; Tielens, A. G. G. M.; Martín, F.; Huber, B. A.; Cederquist, H. *Phys. Rev. Lett.* **2013**, *110*, 185501.

(18) Delaunay, R.; Gatchell, M.; Rousseau, P.; Domaracka, A.; Maclot, S.; Wang, Y.; Stockett, M. H.; Chen, T.; Adoui, L.; Alcami, M.; Martin, F.; Zettergren, H.; Cederquist, H.; Huber, B. A. *J. Phys. Chem. Lett.* **2015**, *6*, 1536–1542.

(19) Ullrich, J.; Moshammer, R.; Dorn, A.; Dörner, R.; Schmidt, L. P. H.; Schmidt-Böcking, H. *Rep. Prog. Phys.* **2003**, *66*, 1463.

(20) Dörner, R.; Mergel, V.; Jagutzki, O.; Spielberger, L.; Ullrich, J.; Moshammer, R.; Schmidt-Böcking, H. *Phys. Rep.* **2000**, *330*, 95 – 192.

(21) Endo, K.; Hoshi, T.; Kobayashi, N.; Miura, H.; Kudo, M. *Polym. J.* **1997**, *29*, 457.

(22) Ida, T.; Sugimoto, H.; Matsumoto, D.; Endo, K. *J. Surf. Anal.* **2005**, *12*, 153.

(23) Endo, K.; Hayashi, K.; Ida, T.; Matsumoto, D.; Kato, N. *J. Surf. Anal.* **2010**, *17*, 2.

(24) Bauer, C. A.; Grimme, S. *J. Phys. Chem. A* **2016**, *120*, 3755.

(25) Karplus, M.; McCammon, J. A. *Nat. Struct. Mol. Biol.* **2002**, *9*.

(26) Karplus, M. *Acc. Chem. Res.* **2002**, *35*, 321–323.

(27) López-Tarifa, P.; Hervé du Penhoat, M.-A.; Vuilleumier, R.; Gaigeot, M.-P.; Tavernelli, I.; Le Padellec, A.; Champeaux, J.-P.; Alcamí, M.; Moretto-Capelle, P.; Martín, F.; Politis, M.-F. *Phys. Rev. Lett.* **2011**, *107*, 023202.

(28) López-Tarifa, P.; Gaigeot, M.-P.; Vuilleumier, R.; Tavernelli, I.; Alcamí, M.; Martín, F.; Hervé du Penhoat, M.-A.; Politis, M.-F. *Angew. Chem. Int. Ed.* **2013**, *52*, 3160.

(29) Maclot, S.; Piekarski, D. G.; Domaracka, A.; Mery, A.; Vizcaino, V.; Adoui, L.; Martin, F.; Alcami, M.; Huber, B. A.; Rousseau, P.; Díaz-Tendero, S. *J. Phys. Chem. Lett.* **2013**, *4*, 3903–3909.

(30) Gu, B.; Smyth, M.; Kohanoff, J. *Phys. Chem. Chem. Phys.* **2014**, *16*, 24350–24358.

(31) McAllister, M.; Smyth, M.; Gu, B.; Tribello, G. A.; Kohanoff, J. *J. Phys. Chem. Lett.* **2015**, *6*, 3091–3097.

(32) Liu, J.; Zhu, T.; Wang, X.; He, X.; Zhang, J. Z. H. *J. Chem. Theory Comput.* **2015**, *11*, 5897–5905.

(33) Herve du Penhoat, M.-A.; Kamol Ghose, K.; Gaigeot, M.-P.; Vuilleumier, R.; Fujii, K.; Yokoya, A.; Politis, M.-F. *Phys. Chem. Chem. Phys.* **2015**, *17*, 32375–32383.

(34) Spezia, R.; Martin-Somer, A.; Macaluso, V.; Homayoon, Z.; Pratihar, S.; Hase, W. L. *Faraday Discuss. Advance Article, http://dx.doi.org/10.1039/C6FD90070D.* **2016**,

(35) Jellinek, J.; Beck, T. L.; Berry, R. S. *J. Chem. Phys.* **1986**, *84*, 2783.

(36) López, M. J.; Jellinek, J. *Phys. Rev. A* **1994**, *50*, 1445.

(37) Beysens, D.; Campi, X.; Pefferkorn, E. *Fragmentation Phenomena*; Les Houches Series; World Scientific, Singapore, 1995.

(38) Gross, D. H. E.; Hervieux, P. A. *Z. Phys. D* **1995**, *35*, 27.

(39) Gross, D.; Madjet, M.; Schapiro, O. *Z. Phys. D* **1997**, *39*, 75.

(40) Calvo, F.; Bonhommeau, D.; Parneix, P. *Phys. Rev. Lett.* **2007**, *99*, 083401.

(41) Sattler, K. *Handbook of Nanophysics: Clusters and Fullerenes*; Handbook of Nanophysics; CRC Press, 2010.

(42) Lebeault, M.-A.; Baguenard, B.; Concina, B.; Calvo, F.; Climen, B.; Lepine, F.; Bordas, C. *J. Chem. Phys.* **2012**, *137*.

(43) Gross, D. H. E. *Rep. Prog. Phys.* **1990**, *53*, 605.

(44) Martinet, G.; Díaz-Tendero, S.; Chabot, M.; Wohrer, K.; Negra, S.; Mezdari, F.; Hamrita, H.; Désesquelles, P.; Padellec, A.; Gardés, D.; Lavergne, L.; Lalu, G.; Grave, X.; Clavelin, J.; Hervieux, P.; Alcamí, M.; Martín, F. *Phys. Rev. Lett.* **2004**, *93*, 063401.

(45) Díaz-Tendero, S.; Hervieux, P.-A.; Alcamí, M.; Martín, F. *Phys. Rev. A* **2005**, *71*, 033202.

(46) Díaz-Tendero, S.; Sánchez, G.; Alcamí, M.; Martín, F.; Hervieux, P.-a.; Chabot, M.; Martinet, G.; Désesquelles, P.; Mezdari, F.; Wohrer-Béroff, K.; Negra, S. D.; Hamrita, H.; LePadellec, A.; Montagnon, L. *Int. J. Mass Spectrom.* **2006**, *252*, 126.

(47) Chen, L.; Martin, S.; Bernard, J.; Brédy, R. *Phys. Rev. Lett.* **2007**, *98*, 193401.

(48) Rentenier, A.; Ruiz, L. F.; Díaz-Tendero, S.; Zarour, B.; Moretto-Capelle, P.; Bordenave-Montesquieu, D.; Bordenave-Montesquieu, A.; Hervieux, P. A.; Alcamí, M.; Politis, M. F.; Hanssen, J.; Martín, F. *Phys. Rev. Lett.* **2008**, *100*, 183401.

(49) Maclot, S.; Delaunay, R.; Piekarski, D. G.; Domaracka, A.; Huber, B. A.; Adoui, L.; Martín, F.; Alcamí, M.; Avaldi, L.; Bolognesi, P.; Díaz-Tendero, S.; Rousseau, P. *Phys. Rev. Lett.* **2016**, *117*, 073201.

(50) Chen, T.; Gatchell, M.; Stockett, M. H.; Alexander, J. D.; Zhang, Y.; Rousseau, P.; Domaracka, A.; Maclot, S.; Delaunay, R.; Adoui, L.; Huber, B. A.; Schlathölter, T.; Schmidt, H. T.; Cederquist, H.; Zettergren, H. *J. Chem. Phys.* **2014**, *140*.

(51) Martín, F.; Politis, M. F.; Zarour, B.; Hervieux, P. A.; Hanssen, J.; Madjet, M. E. *Phys. Rev. A* **1999**, *60*, 4701.

(52) Hervieux, P. A.; Zarour, B.; Hanssen, J.; Politis, M. F.; Martín, F. *J. Phys. B: At., Mol. Opt. Phys.* **2001**, *34*, 3331.

(53) Bréchignac, C.; Cahuzac, P.; Concina, B.; Leygnier, J.; Ruiz, L. F.; Zarour, B.; Hervieux, P. A.; Hanssen, J.; Politis, M. F.; Martín, F. *Phys. Rev. Lett.* **2002**, *89*, 183402.

(54) Bréchignac, C.; Cahuzac, P.; Concina, B.; Leygnier, J.; Ruiz, L. F.; Zarour, B.;

Hervieux, P. A.; Hanssen, J.; Politis, M. F.; Martín, F. *Phys. Rev. A* **2003**, *68*, 063202.

(55) Severin, E.; Freasier, B.; Hamer, N.; Jolly, D.; Nordholm, S. *Chem. Phys. Lett.* **1978**, *57*, 117 – 120.

(56) Schranz, H. W. *The Journal of Physical Chemistry* **1991**, *95*, 4581–4582.

(57) Ray, J. R. *Phys. Rev. A* **1991**, *44*, 4061.

(58) Jellinek, J.; Li, D. *Phys. Rev. Lett.* **1989**, *62*, 241.

(59) Meyer, H. *Annu. Rev. Phys. Chem.* **2002**, *53*, 141.

(60) Watson, J. K. *Mol. Phys.* **1993**, *79*, 943.

(61) Calogeracos, A.; Castillejo, L. *Mol. Phys.* **1993**, *80*, 1359.

(62) Wales, D. *Energy Landscapes: Applications to Clusters, Biomolecules and Glasses*; Cambridge University Press UK; 1 edition, 2004; p 692.

(63) Dumont, R. S. *J. Chem. Phys.* **1991**, *95*, 9172.

(64) Dumont, R. S. *J. Chem. Phys.* **1992**, *96*, 2203.

(65) Calvo, F.; Labastie, P. *Eur. Phys. J. D* **1998**, *3*, 229.

(66) Niiyama, T.; Shimizu, Y.; Kobayashi, T.; Okushima, T.; Ikeda, K. *Physical Review E* **2009**, *79*, 051101.

(67) Fernandez-Pineda, C. *Am. J. Phys.* **1979**, *47*, 814.

(68) Lee, S.-N.; Shih, M.-H. *Linear Algebra Appl.* **1990**, *132*, 93.

(69) Smith, S. C. *J. Chem. Phys.* **1992**, *97*, 2406.

(70) G.Schaftenaar,; Noordik, J. *J. Comput.-Aided Mol. Design* **2000**, *14*, 123–134.

(71) Schmidt, M. W.; Baldridge, K. K.; Boatz, J. A.; Elbert, S. T.; Gordon, M. S.; Jensen, J. H.; Koseki, S.; Matsunaga, N.; Nguyen, K. A.; Su, S.; Windus, T. L.; Dupuis, M.; Montgomery, J. A. *J. Comput. Chem.* **1993**, *14*, 1347.

(72) The General Atomic and Molecular Electronic Structure System (GAMESS). Home Page: `http://www.msg.ameslab.gov/gamess/` (accessed June 23, 2016).

(73) Frisch, M. J.; Trucks, G. W.; Schlegel, H. B.; Scuseria, G. E.; Robb, M. A.; Cheeseman, J. R.; Scalmani, G.; Barone, V.; Mennucci, B.; Petersson, G. A.; Nakatsuji, H.; Caricato, M.; Li, X.; Hratchian, H. P.; Izmaylov, A. F.; Bloino, J.; Zheng, G.; Sonnenberg, J. L.; Hada, M.; Ehara, M.; Toyota, K.; Fukuda, R.; Hasegawa, J.; Ishida, M.; Nakajima, T.; Honda, Y.; Kitao, O.; Nakai, H.; Vreven, T.; Montgomery, J. A., Jr.; Peralta, J. E.; Ogliaro, F.; Bearpark, M.; Heyd, J. J.; Brothers, E.; Kudin, K. N.; Staroverov, V. N.; Kobayashi, R.; Normand, J.; Raghavachari, K.; Rendell, A.; Burant, J. C.; Iyengar, S. S.; Tomasi, J.; Cossi, M.; Rega, N.; Millam, J. M.; Klene, M.; Knox, J. E.; Cross, J. B. et al. Gaussian-09 Revision E.01. Gaussian Inc. Wallingford CT 2009. Home Page: http://www.gaussian.com (accessed June 23, 2016).

(74) Gnuplot: An interactive plotting program. Home Page: `http://gnuplot.sourceforge.net/` (accessed July 7, 2016).

(75) Tabti, M. *World J. Condens. Matter Phys.* **2012**, *02*, 139.

(76) Calvo, F.; Labastie, P. *Chem. Phys. Lett.* **1995**, *247*, 395.

(77) Fosse., R. *Excitation et fragmentation de petits agregats de carbone par impact atomique de haute vitesse*. Ph.D. Thesis. University Pierre et Marie Curie, France 2000.

(78) Tuna., T. *Etude de la fragmentation de molécules d'intérêt astrophysique de type C_nH_m par collision atomique de haute vitesse*. Ph.D. Thesis. University Paris Sud, France 2008.

(79) Chabot, M.; Béroff, K.; Gratier, P.; Jallat, A.; Wakelam, V. *Astrophys. J.* **2013**, *771*, 90.

(80) NIST Mass Spec Data Center. Home Page: `http://webbook.nist.gov/chemistry/` (accessed January 12, 2016).

(81) Schmidt, M.; Kusche, R.; Kronmüller, W.; von Issendorff, B.; Haberland, H. *Phys. Rev. Lett.* **1997**, *79*, 99.

(82) Madjet, M.; Hervieux, P.-A.; Gross, D.; Schapiro, O. *Z. Phys.* **1997**, *39*, 309.

(83) Barnett, R. N.; Landman, U.; Rajagopal, G. *Phys. Rev. Lett.* **1991**, *67*, 3058.

(84) Hock, C.; Bartels, C.; Straß burg, S.; Schmidt, M.; Haberland, H.; Orsay, F.; Aime, L. *Phys. Rev. Lett.* **2009**, *102*, 043401.

(85) Wales, D. J.; Doye, J. P. K.; Dullweber, A.; Hodges, M. P.; Naumkin, F. Y.; Calvo, F.; Hernández-Rojas, J.; Middleton, T. F. The Cambridge Cluster Database.

(86) Naumkin, F. Y.; Wales, D. J. *Mol. Phys.* **1999**, *96*, 1295.

(87) Davis, H. L.; Jellinek, J.; Berry, R. S. *J. Chem. Phys.* **1987**, *86*, 6456.

(88) Raghavachari, K.; Binkley, J. S. *J. Chem. Phys.* **1987**, *87*, 2191–2197.

(89) Van Orden, A.; Saykally, R. J. *Chem. Rev.* **1998**, *98*, 2313.

(90) Béroff, K.; Chabot, M.; Mezdari, F.; Martinet, G.; Tuna, T.; Désesquelles, P.; LePadellec, A.; Barat, M. *Nucl. Instr. Meth. Phys. Res. B* **2009**, *267*, 866.

(91) Chabot, M.; Martinet, G.; Mezdari, F.; Diaz-Tendero, S.; Béroff-Wohrer, K.; Désesquelles, P.; Della-Negra, S.; Hamrita, H.; LePadellec, A.; Tuna, T.; Montagnon, L.; Barat, M.; Simon, M.; Ismaïl, I. *J. Phys. B: At., Mol. Opt. Phys.* **2006**, *39*, 2593.

(92) Chabot, M.; Mezdari, F.; Béroff, K.; Martinet, G.; Hervieux, P.-A. *Phys. Rev. Lett.* **2010**, *104*, 043401.

(93) Béroff, K.; Nguyen-Thi, V. O.; Chabot, M.; Pino, T.; Tuna, T.; Martinet, G.; LePadellec, A.; Dothi, N. *J. Phys: Conf. Ser.* **2012**, *388*, 102062.

(94) Martinet, G.; Chabot, M.; Wohrer, K.; Della Negra, S.; Gardés, D.; Scarpaci, J. a.; Désesquelles, P.; Lima, V.; Díaz-Tendero, S.; Alcamí, M.; Hervieux, P.-A.; Politis, M. F.; Hanssen, J.; Martín, F. *Eur. Phys. J. D* **2003**, *24*, 149.

(95) Schmidt, M.; Baldridge, K.; Boatz, J.; Elbert, S.; Gordon, M.; Jensen, J.; Koseki, S.; Matsunaga, N.; Nguyen, K.; Su, S.; Windus, T.; Dupuis, M.; Montgomery, J. *J. Comput. Chem.* **1993**, *14*, 1347–1363.

(96) Kosimov, D.; Dzhurakhalov, A.; Peeters, F. *Phys. Rev. B* **2008**, *78*, 235433.

(97) Raghavachari, K. *Chem. Phys. Lett.* **1990**, *171*, 249.

(98) Fueno, H.; Taniguchi, Y. *Chem. Phys. Lett.* **1999**, *312*, 65.

(99) Pacchioni, G.; KouteckyÌĄ, J. *The Journal of Chemical Physics* **1988**, *88*, 1066.

(100) Massó, H.; Veryazov, V.; Malmqvist, P.-a.; Roos, B. O.; Senent, M. L. *J. Chem. Phys.* **2007**, *127*, 154318.

(101) Shi, D.; Niu, X.; Sun, J.; Zhu, Z. *J. Phys. Chem. A* **2013**, *117*, 2020.

(102) Massó, H.; Senent, M. L.; Rosmus, P.; Hochlaf, M. *J. Chem. Phys.* **2006**, *124*, 234304.

(103) Diaz-Tendero, S.; Sanchez, G.; Hervieux, P. A.; Alcami, M.; Martin, F. *Braz. J. Phys.* **2006**, *36*, 529.

(104) Kella, D.; Zajfman, D.; Heber, O.; Majer, D.; Feldman, H.; Vager, Z.; Naaman, R. *Z. Phys. D* **1993**, *26*, 340.

(105) Mezdari, F.; Wohrer-Béroff, K.; Chabot, M.; Martinet, G.; Negrâ, S.; Désesquelles, P.; Hamrita, H.; LePadellec, A. *Phys. Rev. A* **2005**, *72*, 032707.

(106) Orlova, G.; Goddard, J. D. *Chem. Phys. Lett.* **2002**, *363*, 486.

(107) Yamaguchi, Y.; Sherrill, C. D.; Schaefer, H. F. *J. Phys. Chem.* **1996**, *100*, 7911.

(108) Liu, H. P. D. *J. Chem. Phys.* **1970**, *53*, 735.

(109) Cui, Q.; Morokuma, K. *J. Chem. Phys.* **1998**, *108*, 626.

(110) Perić, M.; Engels, B. *Chem. Phys.* **1998**, *238*, 47.

(111) Sánchez, J. P.; Aguirre, N. F.; Díaz-Tendero, S.; Martín, F.; Alcamí, M. *J. Phys. Chem. A* **2016**, *120*, 588.

(112) Boyé-Péronne, S.; Gauyacq, D.; Liévin, J. *J. Chem. Phys.* **2006**, *124*, 214305.

(113) Locht, R.; Davister, M. *Chem. Phys.* **1995**, *195*, 443.

Graphical TOC Entry